ACCELERATOR PHYSICS ISSUES AT THE LHC AND BEYOND

Frank Zimmermann
CERN, SL Division
1211 Geneva 23, Switzerland

ABSTRACT

I review the past performance of hadron colliders and their limitations, discuss the accelerator physics challenges faced by the Large Hadron Collider (LHC) now under construction, and, finally, present an outlook into the future, covering upgrades of the LHC as well as a Very Large Hadron Collider.

1 Introduction

This lecture is structured as follows. First, past and future hadron colliders and the effects limiting their performance are reviewed. Then, I discuss the accelerator physics challenges being confronted by the Large Hadron Collider (LHC). Lastly, an outlook onto the future is given, which includes scenarios for an LHC upgrade and the proposed two stages of a Very Large Hadron Collider (VLHC).

1.1 Collider Performance

The two primary parameters characterizing the performance of a collider are its energy and its luminosity. The maximum beam energy of a hadron collider grows linearly with the strength of the magnets and with the ring circumference. The second parameter, the luminosity L, characterizes the reaction rate R. One can write

$$R = L\sigma \tag{1}$$

where σ is the cross section for a particular reaction. The luminosity L is conventionally quoted in units of cm^{-2} s^{-1}. The particle physicists desire a large value of L and, thus, one task of the accelerator physicist is to increase L as much as possible. If one approximates the transverse beam profile by a Gaussian distribution, the luminosity can be expressed in terms of beam parameters as

$$L \approx \frac{N_b^2 n_b f_{\mathrm{rev}} \gamma}{4\pi \epsilon_{x,N} \beta_x^* \kappa} \tag{2}$$

where N_b denotes the number of particles per bunch, n_b the number of bunches per ring, f_{rev} the revolution frequency, γ the particle energy divided by the rest mass, $\epsilon_{x,N}$ the normalized (subindex 'N') horizontal emittance, and $\kappa = \sigma_y/\sigma_x$ the beam-size aspect ratio at the collision point.

The emittance specifies the area in phase space occupied by the beam. A vertical, horizontal, and longitudinal emittance are defined for the three degrees of motion. These are denoted by $\epsilon_{x,N}$, $\epsilon_{y,N}$, and $\epsilon_{z,N}$ (or $\epsilon_{L,N}$). Without diffusion due to scattering processes or synchrotron radiation, the normalized emittances are conserved quantities under acceleration.

More precisely, the emittances are equal to the area of the ellipse in a 2-dimensional phase space which is encircled by a particle launched at an amplitude equal to the rms beam size, divided by π and by the particle rest energy, *e.g.*, in the horizontal plane,

$$\epsilon_{x,N} = \frac{\oint p_x dx}{\pi m_0 c^2} \ , \tag{3}$$

where x and p_x are the horizontal position and momentum of the particle, as viewed at one location in the ring on successive turns, and m_0 is the particle mass.

The *unnormalized* or *geometric* horizontal emittance is defined as $\epsilon_x = \epsilon_{x,N}/(\gamma\beta)$, or, equivalently, as

$$\epsilon_x = \oint x' dx/\pi \ , \tag{4}$$

where $x' \equiv p_x/p_z$ is the slope of the particle trajectory, p_z the longitudinal momentum, and $\beta = v/c$ the velocity in units of the speed of light.

At any given location around in the ring, the emittance is proportional to the square of the rms beam size, *e.g.*, for the horizontal plane at location s we have

$$\sigma_x^2(s) = \frac{\beta_x(s)\epsilon_{x,N}}{\gamma} = \beta_x(s)\epsilon_x \tag{5}$$

where $\beta_x(s)$ is the horizontal beta function. Equation (2) shows that a small beam size corresponds to a higher luminosity, and in view of Eq. (5), this implies a small beta function at the collision point, a small emittance, and a high energy. In particular, Eq. (2) indicates that for a constant normalized emittance, $\epsilon_{x,N}$, and for a constant beta function the luminosity increases linearly with the beam energy.

We mention in passing that Eq. (2) is an approximation because it ignores variations in the beam-beam overlap which may arise from (1) a crossing angle between the two beams, (2) the change of the transverse beam size over the length of the two colliding bunches, also known as the ‘hour-glass effect’, and (3) the change in the optics due to the beam-beam collision. The approximation of Eq. (2) is good, if the crossing angle θ_c is small compared with the bunch diagonal angle σ_x/σ_z, if the bunch length is small compared with the beta functions $\beta^*_{x,y}$ at the collision point, and if the additional tune shift induced by the collision is small.

The primary luminosity limitations of present and future hadron colliders are imposed by a number of effects, each of which constrains one or several of the parameters on the right-hand side of Eq. (2), or even the value of the luminosity, on the left, itself. The most prominent of these effects include:

1. the beam-beam interaction which refers to either the nonlinear or the coherent interaction of the two colliding particle beams, and which is important for all hadron colliders;

2. the number of available particles which is a concern for $\mathrm{p\bar{p}}$ and ion colliders;
3. the emittance growth due to intrabeam scattering, *i.e.*, scattering of the particles inside a bunch off each other;
4. the luminosity lifetime;
5. the heat load inside the cold superconducting magnets due to synchrotron radiation and electron cloud (we will discuss the electron cloud in a later section);
6. the number of events per crossing, which is limited by the capacitiy of the detector; and
7. quenches (transitions into the normal state) of superconducting magnets due to localized particle losses near the interaction region.

In the course of this lecture, we will describe or give examples for all of these effects.

There could be other parameters relevant to the collider performance, for example the beam polarization. However, this option is presently not foreseen for the next and next-to-next generations of energy-frontier machines, *i.e.*, LHC and VLHC, the only exception being the Relativistic Heavy Ion Collider (RHIC) on Long Island, and we will not discuss it here.

1.2 Past and Future

So far 4 hadron colliders have been in operation, namely the ISR, SPS, Tevatron, and RHIC. A 5th is under construction, the LHC.

The CERN ISR started operation in 1970. A double ring ppcollider, it reached a peak luminosity of 2.2×10^{32} cm^{-2}s^{-1} and a maximum beam energy of 31 GeV with coasting beams of 38–50 A current each. The ISR luminosity was limited by space-charge tune shift and spread (due to the defocusing force of the beam field), coherent beam-beam effects, proton-electron two-stream instabilities, pressure bumps, detector background, and accumulation efficiency.[1] The ISR also provided the first $\mathrm{p\bar{p}}$ collisions, and, when operated with bunched beams, it reached a beam-beam tune shift of $\xi = 0.0035$ per interaction point (IP) with 8 crossings.[2] The beam-beam tune shift is a parameter which characterizes the strength of the beam-beam collision, which we will define further below. The ISR first produced the J/ψ particle and the b quark, though these particles were identified among the ISR collision products only after their discovery elsewhere.

The second hadron collider was the CERN $\mathrm{Sp\bar{p}S}$ operating since 1981 at ten times higher energy than the ISR. The $\mathrm{Sp\bar{p}S}$ discovered the W and Z bosons. Its luminosity was limited by beam-beam interaction, loss of longitudinal Landau damping (the term 'Landau damping' refers to the stabilizing effect of a frequency spread within the beam), number of available antiprotons, hourglass effect, and intrabeam scattering.[3] A typical beam-beam tune shift was $\xi = 0.005$ at each of three interaction points.

The FNAL Tevatron is the first collider constructed from superconducting magnets. Colliding-beam operation here started in 1987.[4] Tevatron luminosity is limited by antiproton intensity, beam-beam interaction including long-range effects, luminosity lifetime, number of events per crossing, and intrabeam scattering. The Tevatron reached an antiproton beam-beam tune shift above $\xi = 0.009$. It discovered the b and t quarks.

RHIC at BNL, the first heavy-ion collider, delivers luminosity since 2000. The main limiting factor is intrabeam scattering. Other factors again are beam-beam interaction, luminosity lifetime, and the number of events per crossing.

The Large Hadron Collider (LHC) is scheduled to start operation in 2006. As for the Tevatron, limits will be the beam-beam interaction, luminosity lifetime, and the number of events per crossing. Possibly, in addition, the electron cloud produced by photoemission or beam-induced multipacting,[5] and local magnet quenches induced by the collision products[6] may prove important. The LHC centre-of-mass energy is 14 TeV and its design luminosity 10^{34} cm^{-2}s^{-1}. The LHC will be the first machine where radiation damping is stronger than intrabeam scattering. The scarcity of antiprotons is no longer a problem, as LHC and all future machines will collide protons on protons.

If stronger magnets become available in the future, the LHC energy could be raised, *e.g.*, by a factor of 2. In the following, we call this energy increase, combined with a luminosity upgrade to 10^{35} cm^{-2}s^{-1}, the 'LHC-II'. Finally, there exist design concepts for two stages of a Very Large Hadron Collider (VLHC),[7] reaching an energy of up to 175 TeV centre of mass, and the Eloisatron Project.[8]

Tables 1, 2, and 3 list parameters for all these colliders, except for the ISR and the Eloisatron. The ISR was a rather special machine, whose parameters are not easily compared with the others. The properties of the Eloisatron are similar to those considered for the VLHC.

Table 1. Example parameters for heavy-ion ion colliders: gold collisions at RHIC and lead ions in LHC.

accelerator	RHIC	LHC
ion species	gold	lead
energy per charge E/Z [TeV]	0.25	7
energy per nucleon E/A [TeV]	0.1	2.76
total centre of mass E_{CM} [TeV]	39	1148
dipole field B [T]	3.46	8.4
circumference C [km]	3.83	26.66
no. of bunches n_b	57	608
number of ions per bunch N_b [10^7]	100	6.8
rms beam size at IP $\sigma^*_{x,y}$ [μm]	110	15
IP beta function $\beta^*_{x,y}$ [m]	2	0.5
tune shift per IP $\xi_{x,y}$	0.0023	0.00015
rms bunch length σ_z [cm]	18	7.5
bunch spacing L_{sep} [m]	63.9	124.8
rms transv. emittance $\gamma\epsilon_{x,y}$ [μm]	1.7	1.5
rms longit. emittance ϵ_L/Z [eVs]	0.12	0.2
IBS emittance growth τ_{IBS} [hr]	0.4	9.8
initial luminosity L [10^{27} cm^{-2}s^{-1}]	0.2	1.0
luminosity lifetime τ [hr]	∼10	9.3

Table 2. Example parameters for pp or $\mathrm{p\bar{p}}$ colliders: S$\mathrm{p\bar{p}}$S, Tevatron run IIa ('TeV2a'),[9] and LHC. † The bunches are split in 3 trains, separated by 2.62 μs; ‡ The total LHC dipole heat load is about 0.8 W/m including the electron cloud. *Equilibrium determined by radiation damping and intrabeam scattering. Arrows refer to dynamic changes during the store.

accelerator	S$\mathrm{p\bar{p}}$S	TeV2a	LHC
beam energy E [TeV]	0.32	0.98	7
dipole field B [T]	1.4	4.34	8.39
total energy/beam [MJ]	0.05	1	334
circumference C [km]	6.9	6.28	26.7
number of bunches n_b	6	36	2800
bunch population N_b [10^{11}]	1.7 (p)	2.7 (p)	1.05
	0.8 ($\mathrm{\bar{p}}$)	~1.0 ($\mathrm{\bar{p}}$)	
no. of IPs	3	2	2 (4)
rms IP beam size $\sigma^*_{x,y}$ [μm]	80, 40	32	15.9
rms IP div. $\sigma^*_{x',y'}$ [μrad]	136, 272	91	31.7
IP beta $\beta^*_{x,y}$ [m]	0.6, 0.15	0.35	0.5
beam-beam tune shift / IP $\xi_{x,y}$	0.005	0.01	0.0034
crossing angle θ_c [μrad]	0	0	300
rms bunch length σ_z [cm]	30	37	7.7
bunch spacing L_{sep} [m]	1150	119 †	7.48
SR power P_{SR} [kW]		$< 10^{-3}$	3.6
dipole heat load dP/ds [W/m]		$\ll 10^{-3}$	0.2 ‡
betatron tune Q_β	26	~20	63
rms transv. emittance $\gamma\epsilon_{x,y}$ [μm]	3.75	~ 3	3.75
eq. horiz. emittance $\gamma\epsilon_x^{eq}$ [μm]		$\sim 10^{\star}$	2.03*
longit. emittance ϵ_L (σ) [eVs]	0.11	0.11	0.2
damp. time $\tau_{x,\mathrm{SR}}$ [hr]		1200	52
IBS growth time $\tau_{x,\mathrm{IBS}}$ [hr]	10	50(?)	142
damping decrement per IP [10^{-10}]		0.025	2.5
events per crossing		~6	18
peak luminosity L [10^{34} cm^{-2}s^{-1}]	0.0006	$\sim$ 0.02	1.00
lum. lifetime τ [hr]	9	9	10

1.3 Empirical Scaling

The empirical parameter scaling of past, present and future colliders may give an indication of the design optimization and possibly provide a guidance for the future development.

Figures 1 and 2 illustrate that both the circumference and the dipole field have increased roughly with the square root of the beam energy. This implies that, at least in the past, half of the energy gain has been realized by advances in magnet technology and the other half by expanding the real estate. We note that LHC-II is consistent with the historical trend, whereas for the VLHC a different scaling is assumed.

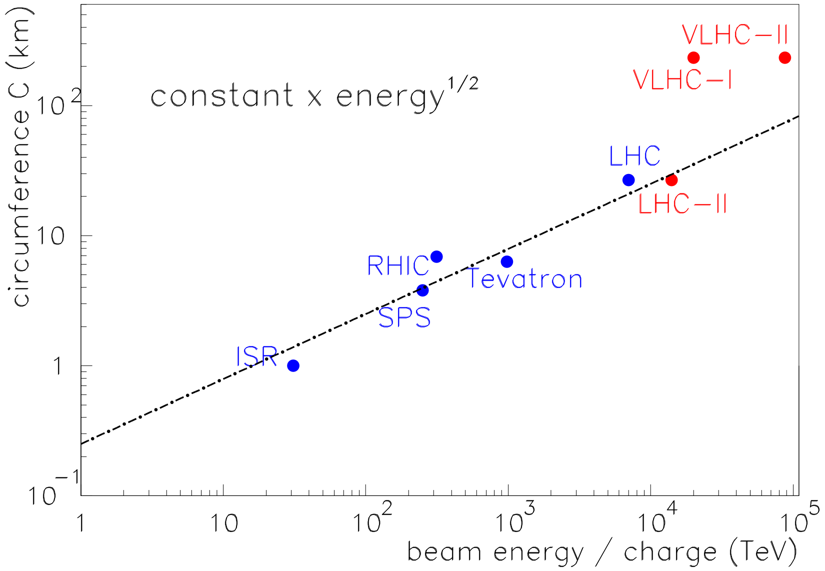

Fig. 1. Ring circumference as a function of beam energy. The solid line indicates the scaling $C \propto \sqrt{E}$.

At the same time, the luminosity has roughly followed the ideal scaling, $L \propto E^2$, as is demonstrated in Figure 3. This would ensure a constant rate of reactions, $R = L\sigma$, in case the cross section decreases inversely with the square of the energy, *i.e.*, $\sigma \propto 1/E^2$.

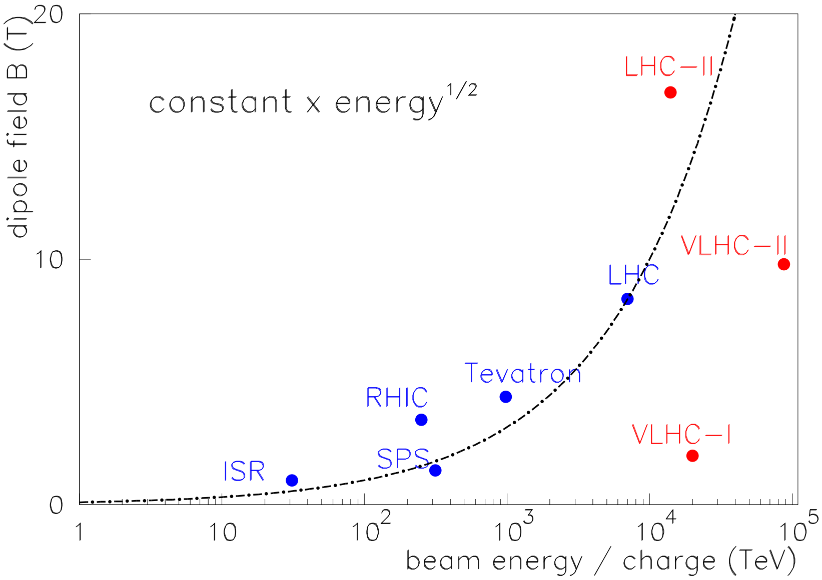

Fig. 2. Bending field as a function of beam energy. The solid line indicates the scaling $B \propto \sqrt{E}$.

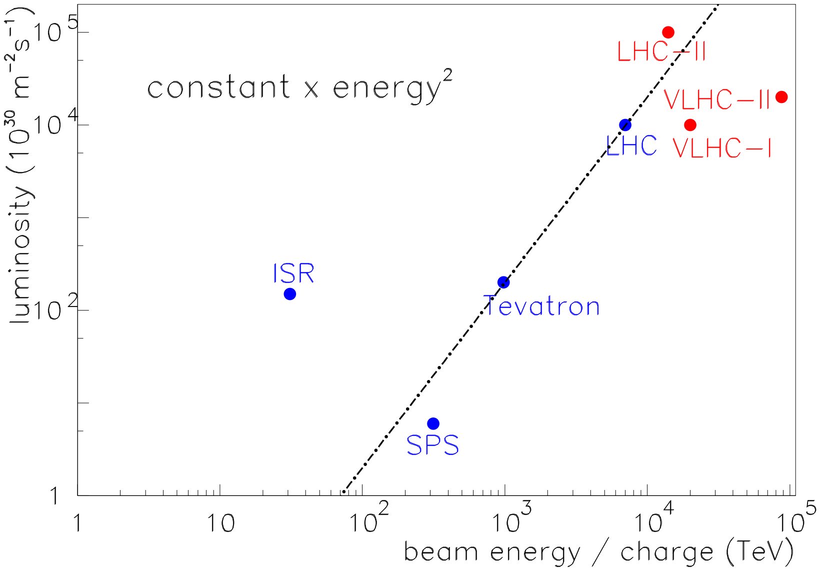

Fig. 3. Luminosity as a function of beam energy. The solid line indicates the scaling $L \propto E^2$.

Table 3. Example parameters for pp colliders: LHC-II, VLHC-I, and VLHC-II. *Assuming a dipole packing factor 0.8 for HF-VLHC, and 0.65 for LHC-II, and ignoring possible contributions from electron cloud. *Equilibrium determined by radiation damping and intrabeam scattering. Arrows refer to dynamic changes during the store. The suffix ‘in’ indicates initial values.

accelerator	LHC-II	VLHC-I	VLHC-II
beam energy E [TeV]	14	20	87.5
dipole field B [T]	16.8	2	9.8
total energy/beam [MJ]	1320	3328	4200
circumference C [km]	26.7	233	233
number of bunches n_b	5600	40000	40000
bunch population N_b [10^{11}]	1.05	0.26	0.075
no. of IPs	2 (4)	2	2
rms IP beam size $\sigma^*_{x,y}$ [μm]	7.4*	4.6	3.4 →0.79
rms IP div. $\sigma^*_{x',y'}$ [μrad]	34*	15	5→1
IP beta $\beta^*_{x,y}$ [m]	0.22	0.3	0.71
beam-beam tune shift / IP $\xi_{x,y}$	0.005	0.002	→0.008
crossing angle θ_c [μrad]	300	153	10
rms bunch length σ_z [cm]	4.0*	3	→1.5
bunch spacing $L_{\rm sep}$ [m]	3.74	5.645	5.645
SR power $P_{\rm SR}$ [kW]	114	7	1095
dipole heat load dP/ds [W/m]	6.6*	0.03	4.7
betatron tune Q_β	63	220	220
rms transv. emittance $\gamma\epsilon_{x,y}$ [μm]	3.75 →1.0	1.5	1.6 →0.04
eq. horiz. emittance $\gamma\epsilon_x^{eq}$ [μm]	1.07*	1.0	0.06
longit. emittance ϵ_L (σ) [eVs]	0.15*	0.4	0.4 →0.1
damp. time $\tau_{x,{\rm SR}}$ [hr]	6.5	200	2
IBS growth time $\tau_{x,{\rm IBS}}$ [hr]	345 (in.)	400	4000→10
damping decrement per IP [10^{-10}]	20	5	400
events per crossing	90	21	54
peak luminosity L [10^{34} cm^{-2}s^{-1}]	10.	1.0	2.0
lum. lifetime τ [hr]	3.2	24	8

1.4 Accelerator Fundamentals

In a storage ring the beam particles execute transverse betatron oscillations as they circulate around the circumference. This is illustrated schematically in Fig. 4. The betatron oscillation with respect to an ideal reference particle on the 'closed orbit' is described by a quasi-harmonic oscillator equation,

$$\frac{d^2x}{ds^2} = -k(s)\,x \tag{6}$$

with the quadrupole focusing force k [m^{-2}]:

$$k = \frac{eB_T}{pa}, \tag{7}$$

where B_T denotes the pole-tip field, a the pole-tip radius of the quadrupole magnet, and p the particle momentum.

The *betatron tune* is defined as the number of betatron oscillations executed per turn. If the betatron tune is near an integer, a particle trajectory will sample a local perturbation on every turn at the same phase of oscillation, and its amplitude may grow until the particle is lost to the chamber wall. Therefore the tune should not be exactly equal to an integer. Similarly, deflections experienced by higher-order fields, *e.g.*, fields with transverse sextupole or octupole symmetry, will accumulate over many turns whenever the horizontal and vertical tunes fulfill the resonance condition

$$kQ_x + mQ_y = p \tag{8}$$

where k, m, and p are integers. In a collider, the largest perturbations of the particle motion usually are the fields of the opposite beam, which 'excite' resonances. The lower the order of a resonance the stronger is its effect. In the CERN S$\mathrm{p\bar{p}}$S collider all resonances of order $(|k| + |m|) \leq 12$ had to be avoided, in order to obtain a good lifetime.

A further complication arises, since the different particles in the beam oscillate at slightly different tunes. The tunes of all particles have to be kept away from the low-order resonances. The beam-beam collision itself, for example, generates such *tune spread*.

Figure 5 shows that the betatron tune Q_β grows with the square root of the circumference, implying a similar scaling for the cell length and the arc beta function.[10] For a constant normalized emittance, the transverse beam sizes in the arc then decrease weakly with beam energy as $\sigma_{x,y\ \mathrm{arc}} \propto 1/E^{1/4}$.

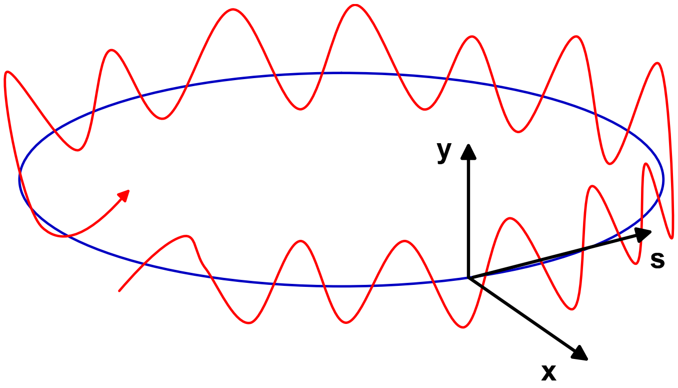

Fig. 4. Schematic of a betatron oscillation in a storage ring. The betatron tune $Q_{x,y}$ is equal to the number of transverse oscillation periods per revolution.

At this occasion, we may recall that the *geometric emittance* refers to the phase space area of the beam distribution, namely

$$\epsilon = \oint x' \, dx \, /\pi \tag{9}$$

where $x'(x)$ is the phase space trajectory of a particle at a transverse amplitude of 1 σ and $x' \equiv dx/ds$ is the slope of the physical trajectory, which here serves as the canonical momentum, and that the *beta function* $\beta_x(s)$ determines the local rms beam size via

$$\sigma_{x,y}(s) = \sqrt{\beta_{x,y}(s)\epsilon_{x,y}}. \tag{10}$$

2 The Large Hadron Collider (LHC)

With 14 TeV centre-of-mass energy, the Large Hadron Collider (LHC) now under construction at CERN will be the highest-energy collider ever built.

In the following, I describe the accelerator physics challenges which are faced by the LHC project. Starting with the choice of machine parameters, and then addressing the issues of superconducting magnets, commissioning schedule, accelerator layout and optics, I proceed to the effects of head-on and long-range beam-beam collisions, and their impact on luminosity and potential loss of Landau damping. Next, I discuss the dynamic aperture, *i.e.*, the particle-orbit stability, at injection, and give a few examples for the ongoing experimental tests of novel beam diagnostics and analysis. I then briefly mention several technical developments, such as power converters, vacuum system,

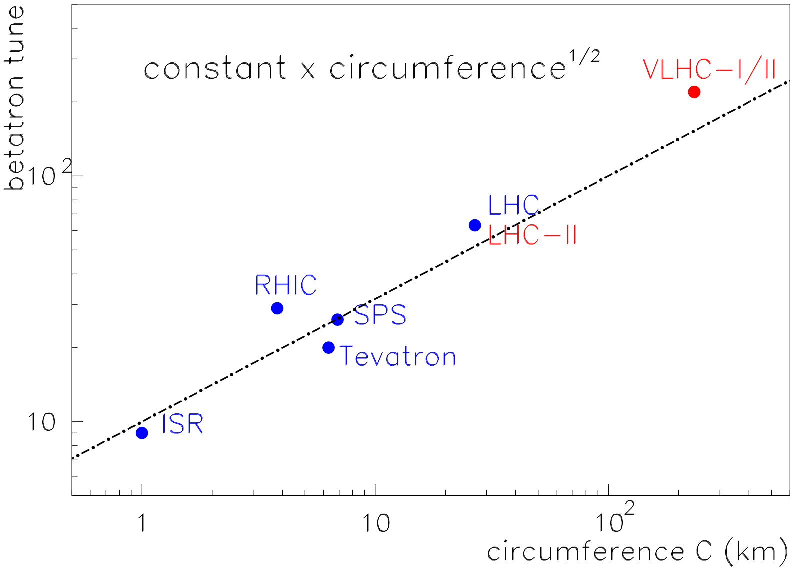

Fig. 5. Betatron tune as a function of the ring circumference.

machine protection and beam dump, including the heat load inside the cold magnets and the requirements for the LHC beam collimation. This is followed by an overview of the LHC injectors and pre-injectors, and the beams they can provide, as well as a brief discussion of luminosity limitations for heavy-ion collisions. Finally, I will describe a new phenomenon that may determine the LHC commissioning strategy and also constrain the ultimate beam parameters, that is the *electron cloud*. This refers to a rapid accumulation of electrons inside the beam pipe during the passage of a bunch train and its consequences.

For more detailed informations on accelerator physics at the LHC, the reader may consult the LHC project web page,[11] the proceedings of the workshops Chamonix X and Chamonix XI,[12] and the web page of the accelerator physics group in the CERN SL Division.[13]

2.1 LHC Parameter Choice

The circumference of the existing LEP tunnel (26.7 km) and the highest possible magnetic field confine the maximum beam energy according to

$$E\ [\mathrm{TeV}] \approx 0.84\ B\ [\mathrm{T}]. \tag{11}$$

For a nominal field B of 8.4 T this yields a beam energy of 7 TeV.

The beam-beam collision induces a betatron-tune spread, whose size is characterized by the beam-beam tune shift parameter ξ. The latter is proportional to the ratio of bunch population N_b and emittance ϵ_x, *i.e.*, $\xi \propto N_b/\epsilon_x$. The maximum tolerable value for the emittance is imposed by the aperture of the magnets, especially at injection.[14] Hence the number of N_b is limited, to about $N_b \approx 1.1 \times 10^{11}$, in the nominal LHC parameter table.

The desired LHC luminosity is $L \approx 10^{34}$ cm^{-2}s^{-1}. Since β_x^*, the beta function at the collision point, cannot be reduced arbitrarily (in particular is should remain larger than the bunch length), and since $\kappa = 1$, the only free parameter in Eq. (2) is the number of bunches n_b. This is chosen as 2808 to match the LHC luminosity target value. The high number of bunches implies a large average beam current, and a high synchrotron radiation power, which has to be absorbed inside the cold magnets.

2.2 Superconducting Magnets

Table 4 shows that the LHC dipoles represent a significant step forward in magnet technology. This is in line with the scaling of Fig. 2. In order to arrive at a compact and cost-efficient design, the LHC magnets are of a new 2-in-1 type where both beam pipes are placed inside the same support structure and cryostat.

Table 4. Dipole magnetic fields in varius hadron colliders. For the Superconducting Super Collider (SSC) only magnet prototypes were built.

accelerator	dipole field
SPS	1.8 T
Tevatron	4 T
HERA	5 T
SSC	6 T
LHC	8.4 T

The heartpiece of the magnets is a superconducting cable, called Rutherford cable, which can support a high current density of 400 A/mm^2, in case of the LHC, to be compared with current densities of order 1 A/mm^2 for normal conductors.[15] The cable itself is made from about 20 strands, each of which consists of hundreds of NbTi filament islands embedded in a copper matrix. The cable is arranged around the beam pipe in a geometry which produces the desired field shape without introducing large errors and nonlinearities. For example, a $\cos\theta$ arrangement yields a pure dipole field. The cable is surrounded by an iron yoke placed inside a non-magnetic collar. Several layers of superinsulation and a vacuum vessel form the outer shell. The first pre-series magnets were delivered to CERN by industry, and have exceeded the nominal field.

2.3 Commissioning Schedule

According to the commissioning schedule as of summer 2001 a complete octant of the LHC will be cooled down and tested in 2004. The last dipole magnet is due to be delivered in March 2005. First beam is foreseen in February 2006, and a 1-month pilot run in April 2006. The first full physics run should start in the fall of the same year. Already for 2007 a few weeks of lead ion collisions are planned.

2.4 Layout and Optics

Figure 6 illustrates the overall layout of the LHC. There are 8 long straight sections. The two largest experiments, CMS and ATLAS, are located in the North and South straight sections, called interaction point 5 (IP5) and 1 (IP1), respectively. The two straight sections adjacent to ATLAS accommodate the experiments LHC-B (IP8) and the ion experiment ALICE (IP2). They simultaneously serve for beam injection. Two of the remaining straight sections are devoted to beam cleaning, another houses the rf, and the last one is needed for beam extraction and dump. The two beams pass alternately thought the inner and outer beam pipe, interchanging their locations in the 4 experimental IPs. Each beam travels for half of the circumference on the outer and the other half on the inner side, such that the revolution times are identical and the beams remain synchronized.

Development of the LHC optics has been a challenging task, as the length of the straight sections was pre-defined by the geometry of the LEP tunnel. In addition, due to a large number of magnets common to both rings, new optics tools had to be developed which allow for a simultaneous ‘matching’ of both rings.

As an illustration of the final achievement, Fig. 7 shows the beta functions $\beta_{x,y}$ and the horizontal dispersion D_x as a function of longitudinal position for beam no. 1 in IP5. The optics in IP1 is basically identical. The optics for beam no. 2 is always the mirror image of that for beam no. 1. The minimum beta functions of $\beta_{x,y} = 0.5$ m

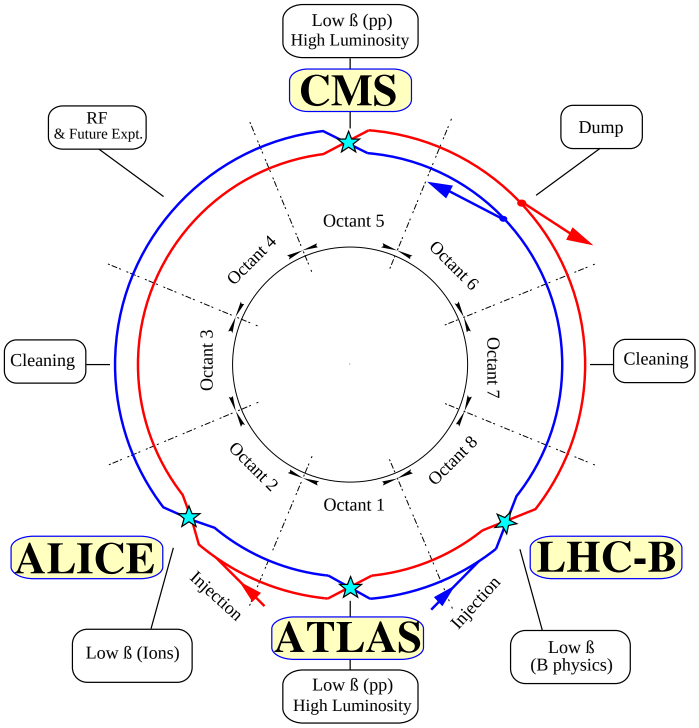

Fig. 6. LHC layout.

are assumed at the collision point (the center of the picture). The dispersion function D_x, which describes the horizontal orbit offset x for a relative momentum error $\Delta p/p$ via the relation $x = D_x(\Delta p/p)$, is almost zero around the collision point. It takes on noticable values only at the entrance to the arcs, on either side of the picture.

Figure 8 displays the orbit in the interaction region. The orbit is not flat, because the bunches collide with an angle, in order to separate them as quickly as possible before and after the main collision point. Otherwise, unwanted collisions with earlier or later bunches of the opposing beam would equally contribute to the beam-beam tune shift and tune spread, and possibly to the background, but not to the luminosity. The nominal full crossing angle is 300 μrad. The orbit of each beam must provide half this angle, as indicated.

Figure 9 shows a top view of magnets around the ATLAS detector (IP1). The collision point is at the center. The beams are focused by superconducting quadrupole triplets, consisting of the three quadrupoles Q1, Q2 and Q3. The free distance between the exit face of the last quadrupole and the collision point is about 23 m. Outside the triplet, a dipole magnet D1 separates the two beams, so that they are guided into the two

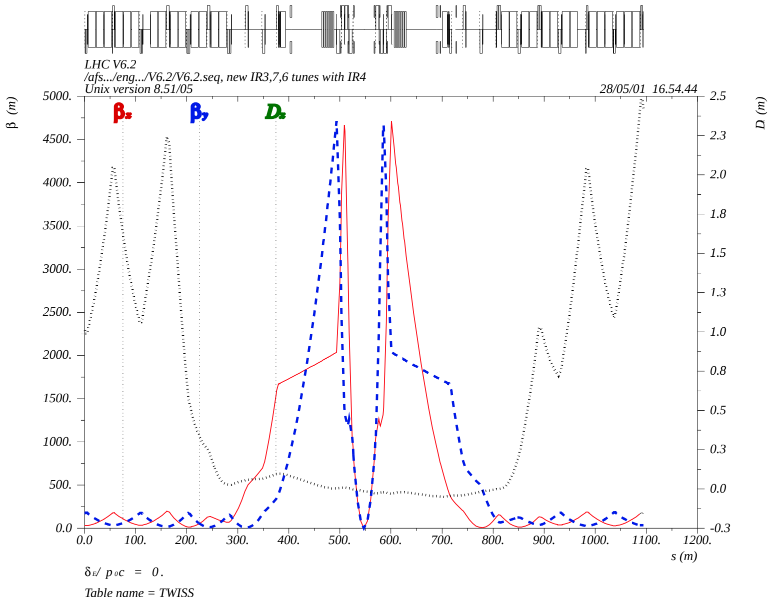

Fig. 7. Collision lattice for beam 1 at IP5. Both beta functions $\beta_{x,y}$ and horizontal dispersion are shown. (Courtesy A. Faus-Golfe, 2001)

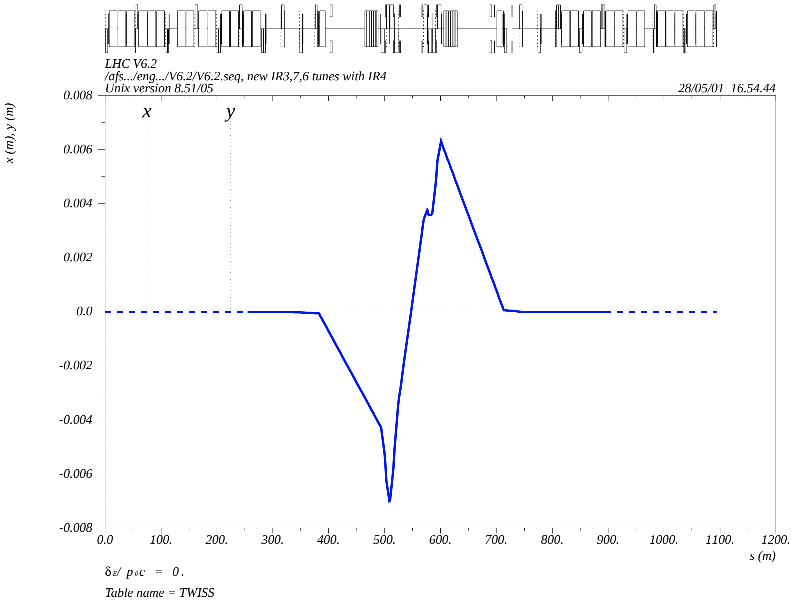

Fig. 8. LHC design orbit for beam 1 near IP5 (CMS) in collision. (Courtesy A. Faus-Golfe, 2001)

beam-pipe channels of the arc magnets. A second dipole D2 further outwards, reverses the deflection imparted by D1, such that the beams are again perfectly aligned in the direction of the arc magnets.

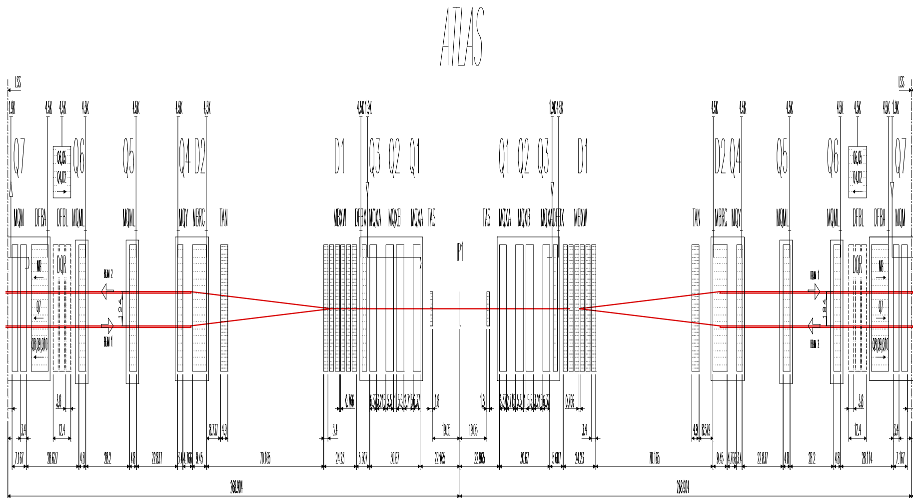

Fig. 9. Magnet layout (top view) around IP 1 (ATLAS). (Courtesy A. Faus-Golfe, 2001)

2.5 Head-On Beam-Beam Collision

In the main collision point, the repelling force of the opposing beam acts like a defocusing lens, as is illustrated in Fig. 10. The defocusing force decreases the betatron tune of all particles. However, for large amplitudes the beam fields decrease inversely with the transverse distance, so that particles at large amplitudes experience a smaller effect than particles near the center of the other beam. The nonlinearity of the beam lens thus induces a tune spread. The maximum acceptable tune spread gives rise to the so-called *beam-beam limit*.

The tune shift and maximum tune spread $\Delta Q_{x,y}$ induced by the collision with the opposing beam is characterized by the beam-beam tune shift parameter:

$$\xi_{x,y} \equiv \Delta Q_{x,y} = -\frac{r_p \beta^*_{x,y} N_b}{2\pi\gamma\sigma^*_{x,y}(\sigma^*_x + \sigma^*_y)}. \tag{12}$$

Note that the horizontal effect of the other beam is similar to that of a single defocusing quadrupole of integrated strength $kl_{\rm quad}$, and that the latter would produce a (horizontal) tune shift

$$\Delta Q_{x,{\rm quad}} \approx \frac{1}{4\pi}\beta_{x,q}\, kl_{\rm quad}, \tag{13}$$

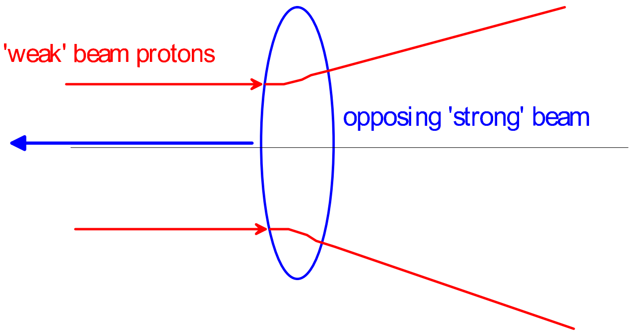

Fig. 10. Schematic of head-on beam-beam collision.

Table 5. Comparison of single-IP and total beam-beam tune shifts for selected hadron colliders.

	SPS	TeV-IIa	LHC
ξ/IP	0.005	0.01	0.0034
$\xi_{\rm tot}$	0.015	0.02	0.009

where k was defined in Eq. (7), $l_{\rm quad}$ is the quadrupole length, and $\beta_{x,q}$ the beta function at the quadrupole. Indeed, Eq. (12) for ξ_x can be derived from Eq. (13), if one replaces $kl_{\rm quad}$ by $-\Delta x'/x$ where $\Delta x'$ denotes the kick imparted by the opposing beam to a particle with a small horizontal offset x.

Table 5 compares the beam-beam tune shift for the LHC with the tune shifts achieved at the SPS and the Tevatron. Both the tune shift per collision point and the total tune shift (adding contributions from all interaction points) are listed. The table demonstrates that either number is smaller for the LHC than what has already been reached elsewhere. In this regard, the LHC parameters appear rather conservative.

The head-on beam-beam tune shift for one IP, given in Eq. (12), can be rewritten as

$$\xi_{x,y} = \frac{r_p N_b}{2\pi\epsilon_{x,N}(1+\kappa)}, \tag{14}$$

where $\kappa = \sigma_y/\sigma_x$ denotes the aspect ratio. Assuming that $\beta_y^*/\beta_x^* = \epsilon_y/\epsilon_x = \kappa$, so that the beam-beam tune shift is of the same value in both planes, $\xi \equiv \xi_x = \xi_y$, we can reexpress the luminosity of Eq. (2) as

$$L = (f_{\rm rev} n_b N_b)\, \frac{1+\kappa}{\beta_y^*}\, \gamma\, \frac{\xi}{2r_p} \tag{15}$$

This demonstrates that there are only four factors which can be optimized for high luminosity: (1) the emittance ratio κ, (2) the IP beta function $\beta_y^* = \kappa\beta_x^*$, (3) the maximum beam-beam tune shift ξ, and (4) the total beam current $(f_{\rm rev} n_b N_b)$.

For flat beams $\kappa \ll 1$ and one finds that the luminosity is half that of the round-beam case, $L_{\rm flat} \approx L_{\rm round}/2$, unless β_y^* can be reduced, which seems more difficult for $\rm pp$ than for $\rm p\bar{p}$ colliders.[16]

2.6 Long-Range Beam-Beam Collisions

Both on the incoming and outgoing side of the IP, each bunch encounters several bunches of the opposing beam, which are transversely displaced due to the crossing angle. The perturbation from these long-range encounters further increases the tune spread and can destabilize particles oscillating at amplitudes of a few σ, *i.e.*, particles which come closer to the other beam during their betatron motion.

Each bunch experiences up to 15 long-range collisions on either side of each head-on interaction point. Bunches with a smaller number of long-range encounters at the head and tail of a bunch train will likely have a poor lifetime. These bunches are therefore called PACMAN bunches,[17] alluding to the computer game of the same name.

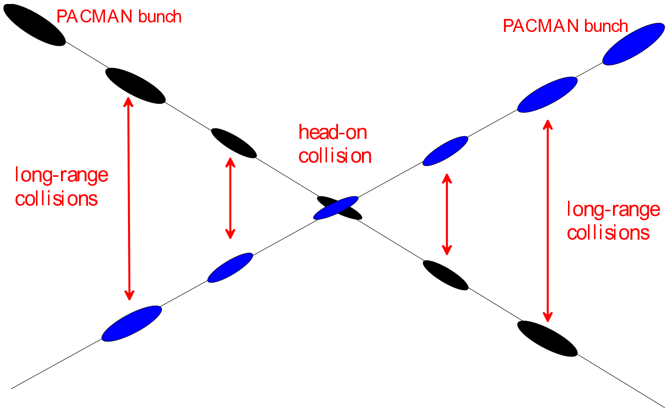

Fig. 11. Schematic of long-range collisions on either side of the main interaction point.

The linear tune shift introduced by the long-range collisions exactly cancels if half of the beam-beam crossings are in the vertical and the other half in the horizontal plane. For this reason the LHC beams will be crossed horizontally at two IPs and vertically at the other two.

However, the higher-order effects of the long-range collisions do not cancel, but instead can cause a strong diffusion at larger betatron amplitudes. Indeed, the LHC will enter a new regime of the beam-beam interaction, where the long-range encounters on either side of the interaction point may be the dominant perturbation, rather than the head-on collisions as in the past colliders.

These long-range collisions give rise to a well defined *diffusive aperture*.[18,19] This diffusive aperture, $x_{\rm da}$, is smaller than the beam-centroid separation at the long-range collision points, $x_{\rm sep}$, by an amount Δ. In other words, we can write

$$x_{\rm da} = x_{\rm sep} - \Delta, \tag{16}$$

where[19,20]

$$\frac{\Delta}{\sigma} \propto \sqrt{\frac{N_b}{\epsilon_N}}. \tag{17}$$

In particular, if quoted in units of the rms beam size σ, the diffusive aperture is independent of the IP beta function and the beam energy.[20] For the nominal LHC parameters, the beams are separated by $x_{\rm sep} \approx 9.5\sigma$ and the diffusive aperture may be as low as $x_{\rm da} \approx 6\sigma$.[19,20]

Figures 12 illustrates the head-on *tune footprint*, as well as the additional tune spreads due to the long-range effects at LHC IP 1 and 5, respectively. These tune footprints show the tunes for particles with transverse amplitudes extending between 0 and 6 times the rms beam size (6 σ). The figure confirms that the alternating crossings in IP1 and IP5 results in a partial cancellation of the long-range tune shifts. Figure 13 compares the total LHC tune spread, due to all 4 collision points, for a nominal bunch and for a PACMAN bunch, *i.e.*, for a bunch which only encounters half of the nominal number of long-range collisions. The total tune spread of the entire LHC beam, including the PACMAN bunches, must fit between harmful resonances in the tune plane. This requirement will limit the maximum achievable tune shift parameter ξ and thus the bunch intensity N_b.

Figure 14 displays further tune footprints, this time extending up to 10 σ, and calculated with and without long-range collisions, head-on collisions, or field errors in the final quadrupoles. The figure demonstrates that for amplitudes larger than a few σ the effect of the long-range collisions is dominant.

Of more immediate concern than the tune spread is the diffusion rate of particles. In unstable (chaotic) regions of phase space, the particle amplitude increases randomly until the particle is lost. Approximately one can describe this behavior as a diffusion in the action variables I_x and I_y, the latter being defined as the square of the horizontal or

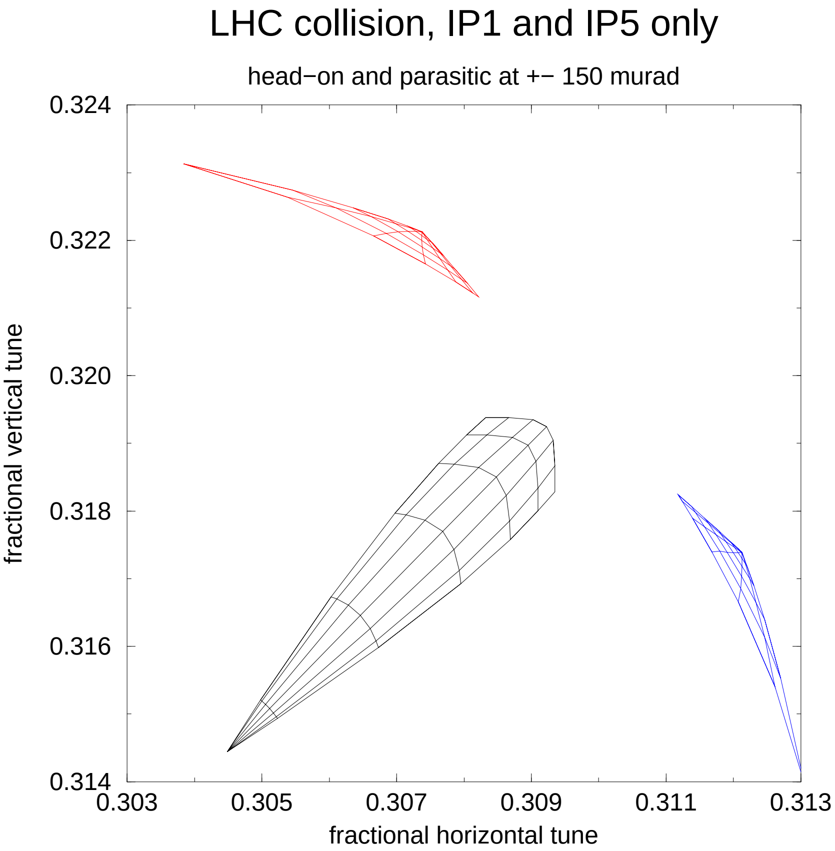

Fig. 12. Tune footprints due to head-on and long-range beam-beam effects in LHC IPs 1 and 5. Vertical axis refers to the vertical tune, horizontal axis to the horizontal. (Courtesy H. Grote)

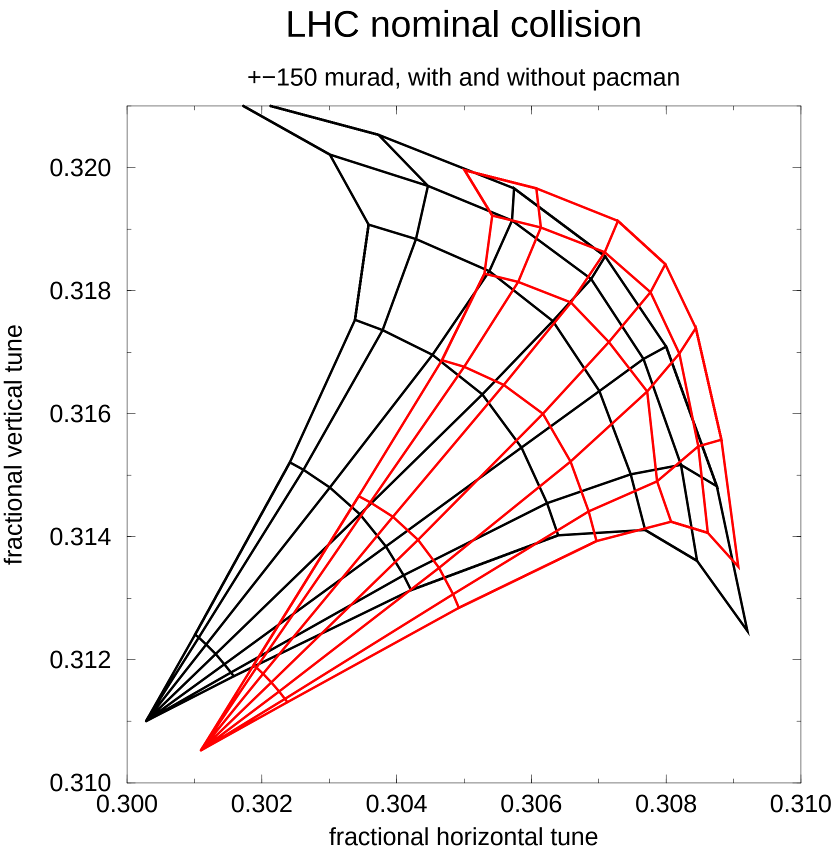

Fig. 13. Total tune footprints in the LHC for a regular bunch and for a PACMAN bunch. (Courtesy H. Grote)

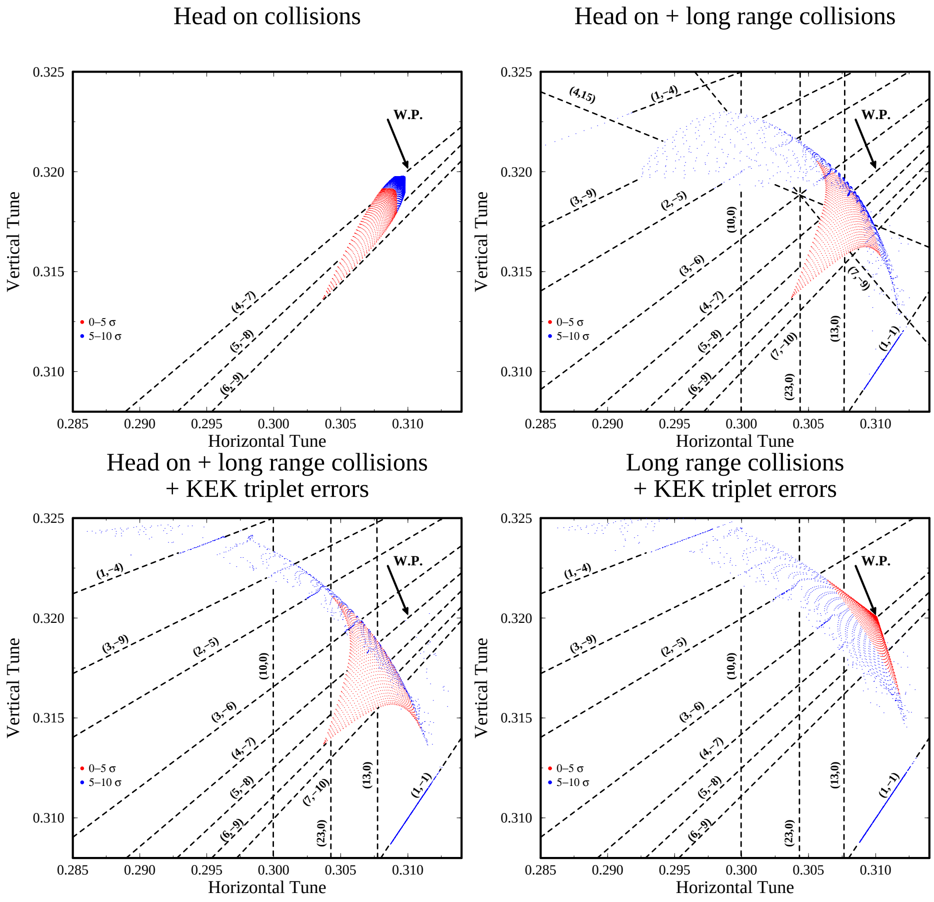

Fig. 14. LHC tune footprints with head-on & long-range collisions and triplet errors.[19] Red dots: x, y_{in} up to $5\sigma_{x,y}$; blue dots: x, y_{in} up to 10 $\sigma_{x,y}$. Top left: head-on collisions only; top right: head-on and long-range collisions; bottom left: head-on plus long-range collisions and triplet (magnet) errors; bottom right: long-range collisions and triplet errors, but no head-on collision.

vertical oscillation amplitude divided by $(2\beta_{x,y})$. In the simulation, the diffusion can be computed by calculating the change in the action variance of a group of particles per unit time.[19] An example is displayed in Fig. 15 for various conditions. Note that the vertical axis has a logarithmic scale. Whenever the long-range collisions are included, the diffusion increases by many orders of magnitude at amplitudes larger than about 6σ. We call this threshold aperture the diffusive aperture. It is due to the long-range conditions. Outside of the diffusive aperture particles will be lost within a few seconds.

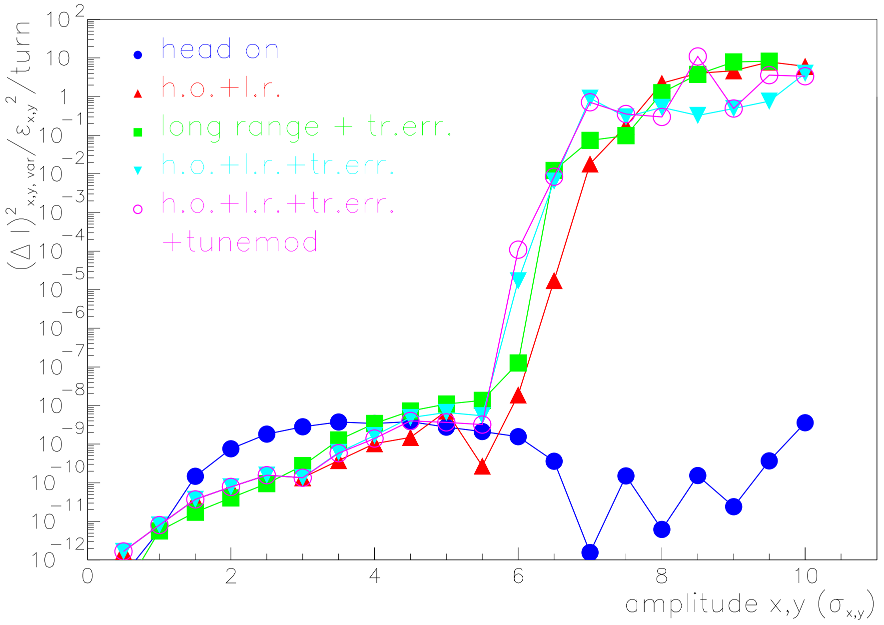

Fig. 15. Change of action variance per turn as a function of starting amplitude in units of the rms beam size, for the LHC.[19] Compared are different combinations of head-on collisions, long-range collisions, triplet-field errors, tune modulation, and even a hypothetical ‘Moebius twist’, where the horizontal and vertical particle coordinates are exchanged on each turn.

Figure 15 presents further simulation results, illustrating the variation of the diffusive aperture with the bunch charge. The right picture summarizes the data on the left-hand side. The simulation confirms that Δ varies with the square root of the bunch population, consistent with Eq. (17). This scaling behavior was first noted by J. Irwin.[18]

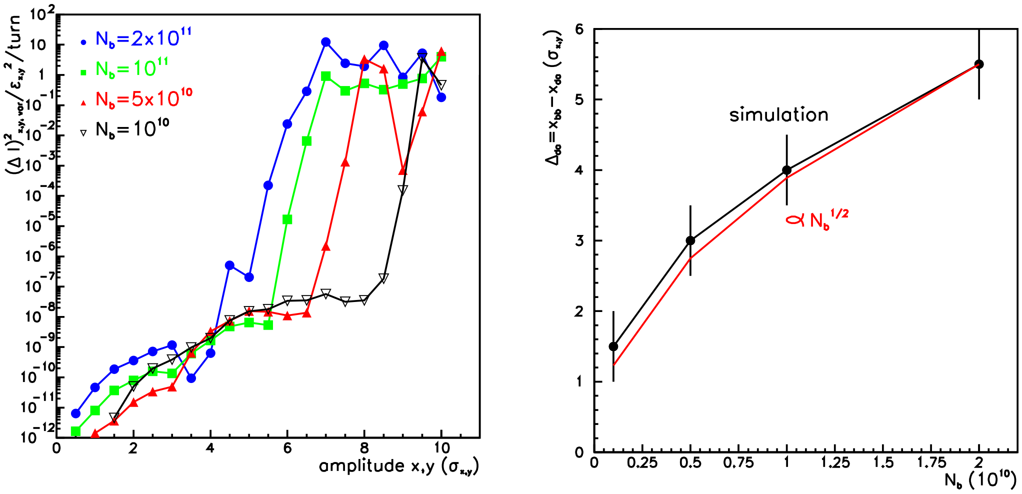

Fig. 16. Dependence of diffusion due to long-range collisions on the beam current.[19] Left: change of action variance per turn vs. bunch population; right: approximate diffusive aperture vs. bunch population; vertical axis describes the distance to the other beam at the parasitic collision points in units of the rms beam size; a square root dependence is also indicated for comparison (dashed line).

2.7 Minimum β^*

A first limit on the IP beta function arises from the hourglass effect. In order to avoid luminosity loss, the IP beta function should be larger than the rms bunch length

$$\beta^*_{x,y} \geq \sigma_z, \tag{18}$$

since on either side of the IP the beta function increases as

$$\beta_{x,y}(s) = \beta^*_{x,y} + \frac{s^2}{\beta^*_{x,y}}, \tag{19}$$

where s denotes the distance to the IP.

A second limit is set by the long-range collisions. As we have just seen, the dynamic aperture caused by parasitic collisions is $x_{\text{da}} \approx (n_{\text{sep}}\sigma - \Delta)$ where n_{sep} is the separation in units of the beam size. For the LHC the separation is chosen as

$$n_{\text{sep}} \geq 9.5, \tag{20}$$

and the simulations indicate that $\Delta \approx 3\sigma$.

If we want to limit the luminosity loss due to the crossing angle, we must demand

$$\theta_c \equiv n_{\rm sep}\sqrt{\frac{\epsilon_{x,y}}{\beta^*_{x,y}}} < 2\,\frac{\sigma_x}{\sigma_z}. \tag{21}$$

Combining Eqs. (20) and (21), we find that

$$\beta^*_{x,y} \geq \frac{n_{\rm sep}\sigma_z}{2} \approx 5\sigma_z, \tag{22}$$

which for the LHC yields $\beta^*_{x,y} > 0.38$ m to be compared with a design value 0.5 m. However, this may not be the full story. Ongoing studies suggest that, if one also includes the constraints from the head-on beam-beam tune shift, it might actually prove advantageous to operate with a crossing angle and an rms bunch length exceeding the limits of Eq. (21) and accept a loss in geometric luminosity, in exchange for a decreased beam-beam tune shift ξ.[21]

Two schemes are presently being explored for compensating the effects of the beam-beam collision. The field of a pulsed electric wire is similar to the beam field experienced at a long-range collision point, and such wire can, therefore, be used to exactly compensate the effect of the long-range encounters. This scheme was proposed by J.-P. Koutchouk.[22] Simulations confirm that a compensating wire is highly effective. An example result is shown in Fig. 17, where the field of the wire increases the diffusive aperture by about 2 σ, even if the betatron phase at the wire location differs by a few degrees from that at the long-range collision points.

A complementary approach is the electon lens built and tested at Fermilab.[23] This lens consists of a low-energy electron beam, which is collided with the antiproton beam. If beta functions and electron current are correctly adjusted, the focusing field of the electrons compensates the focusing force experienced by the antiprotons in the two proton-antiproton collision points. In order to obtain a controllable compensation in both transverse planes, two lenses at locations with different beta functions are needed. If the electron current is modulated, the central tune shift of each bunch can be controlled independently, thereby avoiding PACMAN bunches. Transverse shaping of the electron beam profile should even allow reducing the beam-beam tune spread inside the bunch. The interaction takes place in a strong longitudinal solenoid, in order to suppress transverse two-stream instabilities, which otherwise might develop. During a first beam test in the spring of 2001, the electron lens successfully changed the tune of the Tevatron proton beam by about 0.005, in accordance with the prediction.

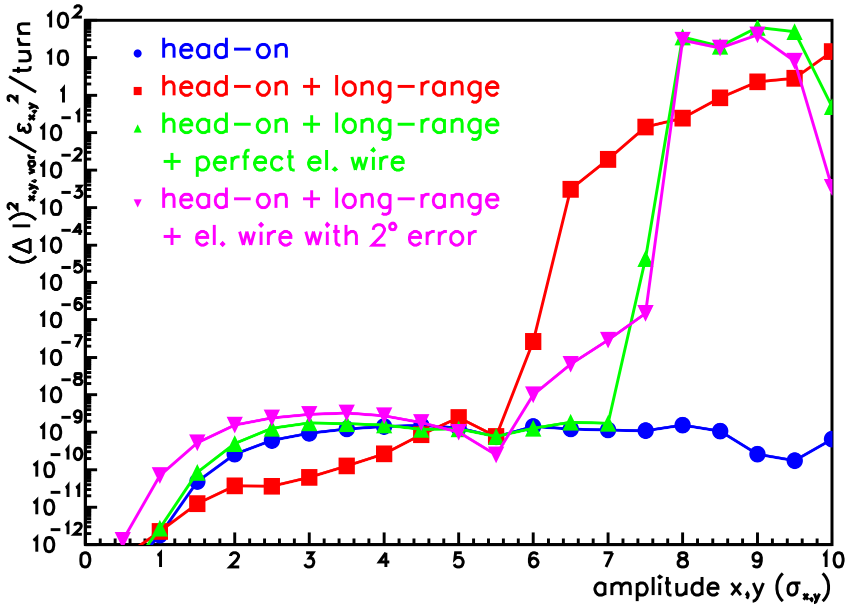

Fig. 17. The diffusion in action variance per turn as a function of the start amplitude, illustrating the effect of an electric wire which mimics long-range encounters of opposite charge.

2.8 Strong-Strong Beam-Beam Effects at LHC

In addition to the effect of a strong opposing beam on a single particle in the other beam, which we have considered above, there also exist strong-strong beam-beam effects, *i.e.*, effects where a collective motion develops due to the coherent interaction of the two beams.

In the case of two colliding bunches two coherent modes are observed: the σ or 0 mode, for which the oscillations of the two bunches are in phase, and the π mode, where the bunches oscillate in counter-phase. These two modes are illustrated for a coupled pendulum in Fig. 18. The oscillation frequency of the σ mode is equal to the unperturbed betatron tune, whereas the frequency of the π mode is shifted downwards (in LHC) by an amount $\Delta Q = Y\xi$. The amount of the downward tune shift is proportional to the tune-shift parameter ξ. The coefficient Y, of the order 1.2–1.3, is sometimes called the Yokoya factor or the Meller-Siemann-Yokoya factor.^{24,25}

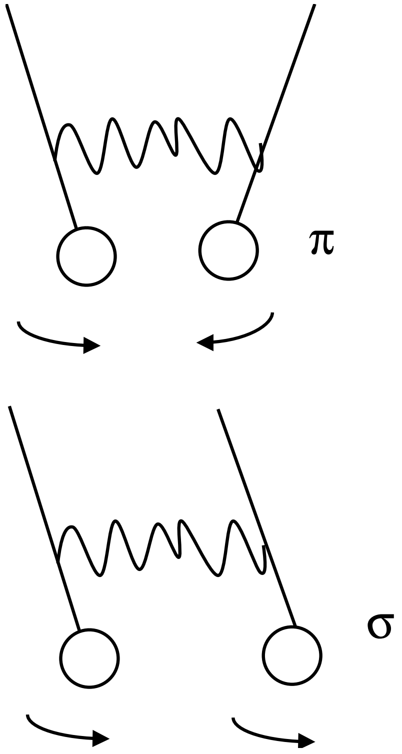

Fig. 18. Simple Model of π and σ modes for a system of two coupled oscillators.

For the following we need to introduce the notion of *Landau damping*. This refers to the phenomenon that a spread of oscillation frequencies of individual particles tends to stabilize the coherent beam motion of the particle ensemble against excitation frequencies within the frequency spread. An illustration employing three swings with either equal or different frequencies on the same support is shown in Fig. 19.

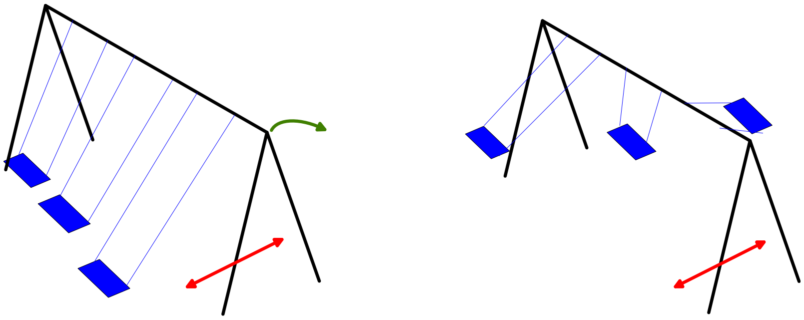

Fig. 19. Schematic of Landau damping, from A. Hofmann.[26]

Mathematically, the driven particle motion is described by

$$\ddot{x} + \omega^2 x = A e^{-i\Omega t}. \tag{23}$$

If the eigenfrequencies ω of many particles are distributed according to a density $\rho(\omega)$, the centroid response of the particle ensemble to the external perturbation $A\exp(-i\Omega t)$ is[27]

$$< x >= \frac{A}{2\bar{\omega}} e^{-i\Omega t} \int d\omega \, \frac{\rho(\omega)}{\omega - \Omega - i\epsilon} \tag{24}$$

where $\epsilon \longrightarrow 0^+$.

For LHC worriesome is a prediction by Y. Alexahin,[28] according to which the coherent π mode in the LHC will not be Landau damped. His argument is that, for bunch intensities of the two beams which are equal to within 40%, the frequency shift of the coherent π mode is larger than the incoherent beam-beam tune spread ξ. A possible reason why this loss of Landau damping was not observed in the SPS or Tevatron is that the antiproton intensities in these machines were always much smaller than the proton intensities, as can be seen in Table 6.

Table 6. Comparison of bunch intensity ratios in SPS, TeV-II and LHC.

	SPS	TeV-II	LHC
intensity ratio N_1/N_2	2	$9 \rightarrow 2$	1

The original argument[28] applied to the head-on collision only. It was speculated that the long-range collisions may act either stabilizing or de-stabilizing. Extensive simulation studies by M. Zorzano[29,30] support Y. Alexahin's predictions, and do show the loss of Landau damping. An example simulation result is shown in Fig. 20. These simulations also indicate that the long-range collisions will not stabilize the π mode. Further analytical work by Y. Alexahin has since confirmed this conclusion.

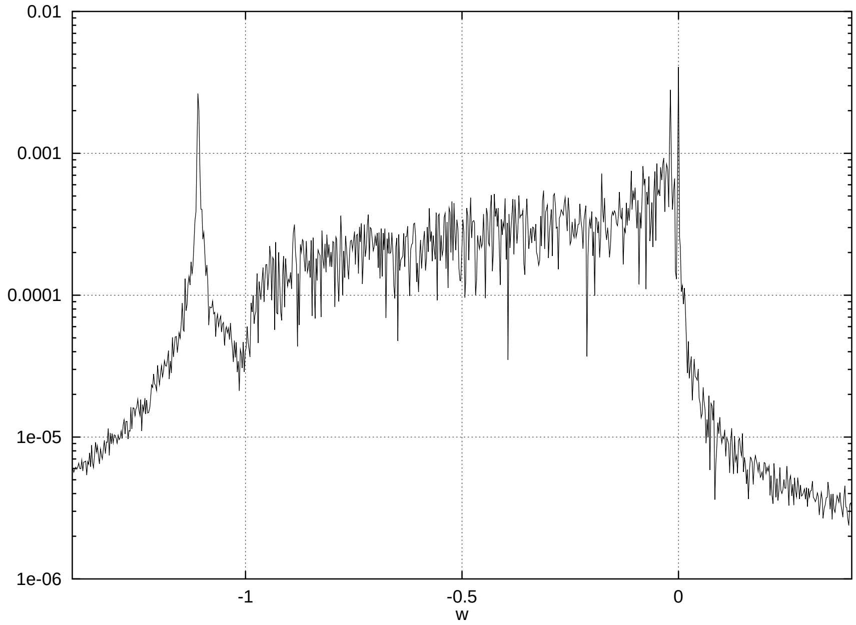

Fig. 20. Simulation of coherent modes (M. Zorzano): frequency spectrum of the bunch centroid motion; vertical axis is on a logarithmic scale with arbitrary units, plotted along the horizontal axis is the normalized frequency $w = (\nu - Q)/\xi$. The π- and σ-oscillation modes are clearly visible.[29,30]

A possible cure suggested by A. Hofmann is to separate the tunes in the two rings. Simulations for separated tunes suggest that Landau damping may be restored, provided that the betatron tune split between the two rings is larger than the beam-beam tune shift. However, at most or all of the alternative asymmetric working points higher-order coherent resonances may be encountered.[30]

Both theory and simulations rely on various approximations and assumptions. Experimental studies of the π mode stability have been performed in LEP, where the π mode was clearly observed, and are planned at RHIC.

2.9 Single-Bunch Collective Effects

There are a number of single-bunch collective effects. They all are driven by the impedance of the vacuum chamber, *i.e.*, by electro-magnetic fields excited by the beam and acting back on it. Here we do not discuss these effects in detail, but merely mention the most important ones.

The coherent synchrotron tune shift with intensity (the synchrotron tune describes the longitudinal oscillation frequency and is defined in analogy to the betatron tune for the transverse plane) may cause a loss of Landau damping at high bunch intensity.[31,32] A possible countermeasure is the controlled blow up of the longitudinal emittance. For a longer bunch the synchrotron frequency spread increases due to the nonlinearity of the sinusoidal rf wave in the rf cavities.

The predicted threshold of the longitudinal microwave instability is far above the nominal LHC parameters. Similarly, the calculated threshold for transverse mode coupling at injection of $N_b \approx 5.9 \times 10^{11}$ is safely above the design current.

The transverse resistive wall instability is important, however. For the nominal LHC parameters the growth time of the lowest multi-bunch mode is $\tau \approx$ 30 ms, which corresponds to 300 turns; for twice the number of bunches and the ultimate bunch population (1.7×10^{11}) it decreases to $\tau \approx$ 10 ms or 100 turns.

The tune shift variation for a partially filled ring due to the ac magnetic field leakage and a finite resistive wall is a small effect, as shown by J. Gareyte.[33]

Incoherent tune shift due to collective fields was recognized as a potential problem for the VLHC.[34,35] It might also be noticable at the LHC. For the nominal LHC parameters at injection the incoherent tune shift is $\Delta Q_y \approx 0.02$; for higher intensity it may approach $\Delta Q_y \approx 0.07$. This could cause potential problems such as (1) a reduction of dynamic aperture, or (2) resonance crossings of the coherent multi-bunch modes.

2.10 Dynamic Aperture at Injection

Nonlinear field errors can destabilize particle motion after 1000s of turns. Error sources include persistent currents (eddy currents in the superconductor), the geometry of the superconducting coil, and the current redistribution during acceleration.

The maximum stable area in phase space is called the *dynamic aperture*. The approach that was taken to guarantee a sufficiently large dynamic aperture for the LHC consisted of three parts[36]: (1) computer simulations of the particle motion under the influence of nonlinear field errors were performed over 10^6 turns, (2) the computer simulation were calibrated against measurements at the SPS and HERA, which showed that the simulation and measurements deviate at most by a factor of two, and (3) a 12σ dynamic aperture was required in the simulation, so as to assure that the actual aperture will be larger than 6σ.

2.11 Persistent Currents

The persistent currents decay during injection. This will cause a change in chromaticity Q' by some 300 units, due to a change in the sextupole fields generated by the persistent currents. Here, the chromaticity is defined as the change in betatron tune ΔQ per relative momentum error $\Delta p/p$. At the start of acceleration the eddy currents are rapidly reinduced, within 100 s, and the chromaticity accordingly changes back to its initial value. This is called the '*snap-back*'. A chromaticity of several hundred units would imply a tune spread of the order 1, clearly unacceptable. In order to maintain a good beam lifetime and large dynamic aperture, the chromaticity must be controlled to within about 5 units.

The strategy to cope with the decay and snap-back is twofold. First, it is important that the acceleration starts slowly and reproducibly. Precise digital controllers for the LHC main power converters have been designed and built to accomplish this goal,[37] and an optimized excitation curve has been computed.

Second, new diagnostics enabling a fast measurement of chromaticity for immediate correction was developed and has already been tested at the CERN SPS. This is discussed next.

2.12 Novel Diagnostics

The conventional way of measuring the chromaticity is to detect the tune variation with rf frequency. This technique is rather time consuming.

A new method invented for the LHC measures the change in the phase of the betatron oscillation at the head and tail of a bunch following a kick excitation,[38] as illustrated in Fig. 21. If the chromaticity is zero, the head and tail always oscillate in phase. If the chromaticity is nonzero, on the other hand, a phase shift builds up between head and tail due to the integrated energy difference between particles passing these two locations during their slow oscillations in the longitudinal phase space. The longitudinal oscillations are called synchrotron oscillations, and the associated tune is called the synchrotron tune Q_s. The value of Q_s is much smaller than the betatron tunes. In the LHC at injection, it is 0.006.

In the new chromaticity measurement, the phase difference which emerges between head and tail is proportional to the chromaticity. It is maximum after half a synchrotron period, and decreases again to zero after a full period.

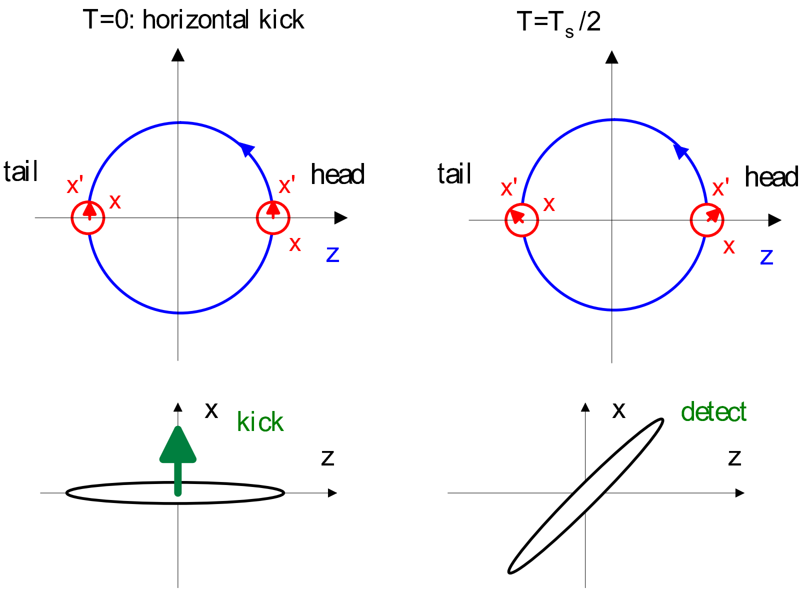

Fig. 21. Principle of chromaticity measurement via head-tail phase shift.[38]

The chromaticity inferred at turn n after the kick is

$$Q'_{x,y} = \frac{\eta \, \Delta\phi(n)}{\omega_0 \Delta\tau (\cos(2\pi n Q_s) - 1)}, \tag{25}$$

where $\Delta\phi(n)$ is the head-tail phase difference measured at the nth turn, $\Delta\tau$ the difference in arrival time between head and tail, and η the slippage factor, an optical parameter that can be calculated analytically ($\eta \equiv \alpha_c - 1/\gamma^2$ is defined as the relative change in revolution time per relative momentum change, and α_c is the so-called momentum compaction factor).

In principle, this technique might measure the chromaticity in about 10 ms, which is much shorter than the time scale of the snap back. A test measurement using a wideband pick up at the SPS is shown in Fig. 22.

Another diagnostics which has been developed in view of LHC is the processing of data from multi-turn beam-position monitors (BPMs) taken after deflecting a bunch to

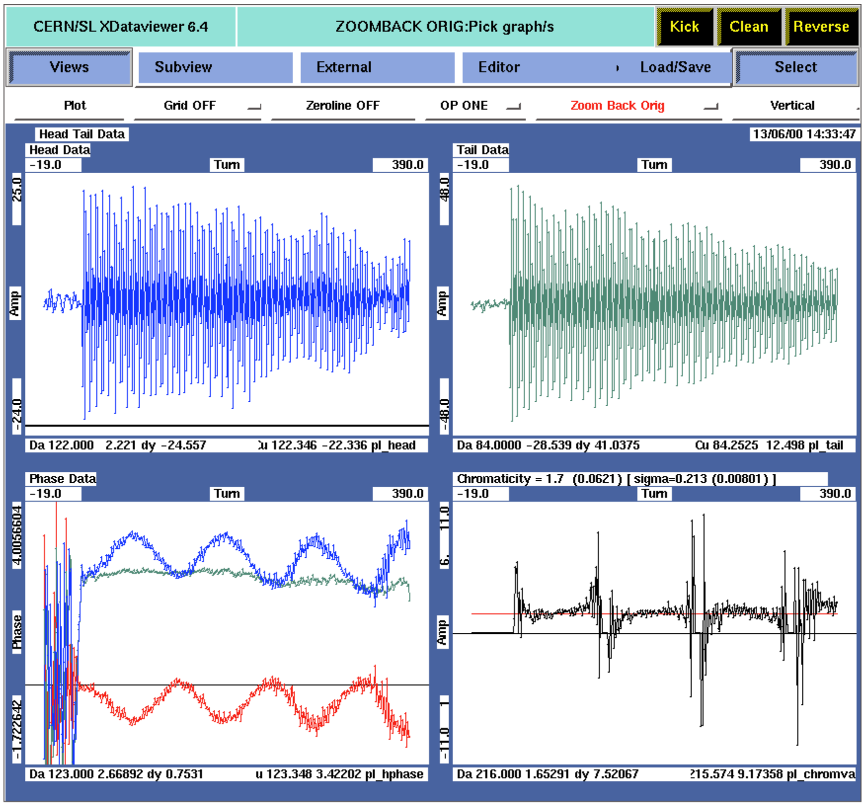

```
Da 122.000   2.221 dy -24.557            Cu 122.346 -22.336 pl_head
Da 84.0000 -28.539 dy 41.0375            Cu 84.2525  12.498 pl_tail
Chromaticity = 1.7  (0.0621) [ sigma=0.213 (0.00801) ]
Da 123.000 2.66892 dy 0.7531             u 123.348 3.42202 pl_hphase
Da 216.000 1.65291 dy 7.52067            215.574 9.17358 pl_chromva
```

Fig. 22. Chromaticity measurement via head-tail phase shift in the SPS.[38] Top: raw oscillation data of bunch head and bunch center, bottom left: individual phases and phase difference $\Delta\phi$ (red), bottom right: inferred chromaticity. (Courtesy R. Jones, 2000)

a large amplitude, so as to extract informations about the nonlinear resonances and to localize nonlinear field errors all around the machine.[39]

The basic idea is to identify for each line in the position Fourier spectrum the corresponding higher-order resonance. From the relative height of such lines, their variation with the kick amplitude, and their change from one BPM to the next, informations can be obtained which may allow identifying problematic regions in the ring and minimization of the residual nonlinearities, thereby maximizing the dynamic aperture.

2.13 Power Converters

The LHC power converters were newly developed to meet the stringent demands on resolution, stability, and accuracy. The power converters for the main bending magnets and quadrupoles have demonstrated a resolution of 1 ppm.[37] Stability over a day is of the order of 5 ppm.[37]

2.14 Heat Load inside the Cold Magnets

Four primary sources of heat load have been identified, and require special remedies.

The first are lost beam particles. These can be particles which are scattered either off the other beam at the collision point or off residual gas nuclei. Another possibility are particles on unstable trajectories diffusing outwards.

In order to limit the rate of particle losses inside the cold magnets, halo collimation is performed in two straight sections which accommodate warm magnets. Complementarily, the cold magnets are cooled by superfluid helium at 1.9 K, which at this temperature has a remarkable heat capacity.

The second source of heat load is synchrotron radiation. For a bunch intensity of $N_b \approx 1.6 \times 10^{11}$, the synchrotron radiation amounts to about 0.27 W/m. This radiation does not directly shine onto the 1.9-K cold bore, but it is intercepted by a beam screen at a higher temperature varying between 4 and 20 K.

A third source are beam image currents in the resistive chamber wall. For the ultimate bunch intensity $N_b \approx 1.6 \times 10^{11}$, this contributes about 0.46 W/m. Also here the beam screen absorbs most of the heat. The screen is coated with a thin Cu layer to improve the surface conductivity.

A fourth source is the electron cloud, *i.e.*, electrons, generated by photoemission from synchrotron radiation or by secondary emission, which are accelerated in the field of the beam. The heat deposited on the walls by these electrons should not exceed the residual cooling capacity, after accounting for the image-charge effects and direct synchrotron radiation. For $N_b \approx 1.6 \times 10^{11}$, the heat load due to the electron cloud must stay below 0.56 W/m.

2.15 Thermodynamic Considerations

Heat capacities C of the various magnet components have a strong influence on the quench limit. The heat capacity relates the temperature rise ΔT to the energy deposition ΔU per mass Δm via

$$\Delta T = \frac{1}{C} \frac{\Delta U}{\Delta m}. \tag{26}$$

For copper at 1.9 K, the heat capacity is only $C_{\mathrm{Cu}} \approx 0.03$ J/kg/K, which could easily give rise to premature quenches. To raise the quench limit, in the LHC magnets the s.c. cable is permeated by superfluid helium at 1.9 K, whose heat capacity is much higher than that of copper, *i.e.*, $C_{\mathrm{He}} \approx 4000$ J/kg/K.[36] With a measured helium content in the s.c. cable of $\sim 4.5\%$, the average heat capacity is significantly increased.[40] The helium absorbs deposited energy and transports it away from the magnet coils.

Another important point to recall is the refrigeration (Carnot) efficiency, which is given by

$$\eta = \frac{T_{\mathrm{cold}}}{T_{\mathrm{warm}}} \ , \tag{27}$$

and relates the optimum (minimum) power P_{warm} required at room temperature for absorbing a heat influx P_{cold} at a lower temperature:

$$P_{\mathrm{warm}} = \frac{P_{\mathrm{cold}}}{\eta} = \frac{T_{\mathrm{warm}}}{T_{\mathrm{cold}}} P_{\mathrm{cold}}. \tag{28}$$

It is evident that the absorption of heat at $T_{\mathrm{cold}} = 1.9$ K is not efficient. For this reason, a beam screen at higher temperature (4–20 K) is installed inside the magnets, which absorbs the proton synchrotron radiation power as well as the energy from the electron cloud. Two rows of pumping slots on either side — *i.e.*, horizontally outwards or inwards — of the beam-screen center connect the beam vacuum with the cold bore of the magnets, which is held at 1.9 K. This arrangement also enables a highly efficient cryopumping, where desorbed gas molecules diffuse through the pumping slots and then stick to the cold part of the magnet.

2.16 Quench Limits and Collimation

If too many protons are lost in a superconducting magnet, it will *quench*, which means it will become normal conducting. Then the machine protection system acts, and the beam will be dumped. Recovery from a quench is time consuming, and the number of quenches should therefore be minimized, ideally avoided. Taking into account the contributions to the heat capacity from the superfluid helium, the quench limit of an LHC magnet corresponds to a local temperature increase of 7 K at injection and 1 K at top energy.

A quench can be generated by local proton losses. Proton loss mechanisms include[41] (1) injection errors, where the losses occur within a few turns, (2) protons outside of the rf bucket which are lost at the start of the ramp in a 'flash', and (3) continuous losses in collision.

Table 7 compares the expected losses with the quench limit. In view of these numbers, a dedicated beam cleaning system is considered as indispensible for the LHC.

Table 7. Expected total losses and quench limit.[41]

process	exp. total losses	quench limit
injection	$\Delta N = 1.25 \times 10^{12}$	$\Delta N_q = 10^9$ m^{-1}
ramping	$\Delta N = 9 \times 10^{12}$	$\Delta N_q = 2.5 \times 10^{10}$ m^{-1}
collision	$\dot{N} = 3 \times 10^9$ s^{-1}	$\dot{N}_q = 6 \times 10^6$ m^{-1}s^{-1}

The chosen design is a 2-stage system, consisting of primary and secondary collimators.[41]

The primary collimation comprises 3 betatron collimators at an amplitude of 6σ and 1 energy collimator. Each of these is followed by a set of three secondary collimators at an amplitude of 7σ. The collimation inefficiency sensitively depends on the ring aperture $A_{\rm ring}$;

If $A_{\rm ring} = 8\sigma$, the efficiency is about $\eta_{\rm coll} \approx 10^{-4}$, which means that from 10^4 protons in the beam halo, all but one are intercepted by a collimator, before hitting the beam pipe.

At the LHC the collimation must be in the working position already at injection, and all through the acceleration. The tolerance on the dynamic closed orbit stability is rather stringent, namely < 30 μm ($1/10\sigma$), and must be met at all times. This condition assures that the secondary collimators are in the shadow of the primary collimators.

2.17 Machine Protection

The total energy stored in the LHC magnets is about 11 GJ, and the LHC beam energy is 0.7 GJ.[42] These amounts of energy, if liberated in an uncontrolled way, could cause a considerable damage to the machine components. Therefore, a reliable machine protection system is crucial.[42]

There are many aspects to the protection system. We mention only two.

In case of a magnet quench, the ensuing resistive heating further increases the temperature and the rapid heating could destroy the magnet. In order to avoid this, quench heaters will be fired, which induce additional quenches in the adjacent magnets and distribute the energy dissipation over a larger region. At the same time, switches are activated, so that the main current bypasses the region of the quench.

However, the heartpiece of the machine protection is the beam dump. Since the rise time of the extraction kickers is finite and long, an adequately long gap in the stored LHC beam is needed. The kickers can only be fired during this gap, since otherwise several bunches would be deflected by the rising edge of the kicker pulse to intermedate amplitudes without being extracted, and these bunches would damage the collimators or some magnets.

The protection philosophy is that whenever an error is detected, *e.g.*, the beam deviates too much from its nominal orbit, the beam is extracted from the ring and sent onto the dump, before it can destroy any machine components.

The design of the beam extraction system is itself not simple, since the beam density is so high that it can also destroy the beam dump. To prevent this, the extraction system comprises several dilution kickers which deflect the beam in both transverse planes and are activated at the same time as the extraction kickers.[43] Different bunches are deflectd by different amounts, such that the bunch impact point on the entrance face of the beam dump traces a nearly circular path over the length of the bunch train. The diameter of the sweep profile is about 15 cm, which provides for sufficient dilution of the beam density.[43]

The extraction kickers consist of many units. The most serious conceivable failure mode in the LHC is the accidental spontaneous firing of one of these kicker units. The protection system will then also fire all other kicker modules, in order to sent the beam to the dump. However, in this case the kick is not synchronized with the position of the beam gap, and component damage due to the impact of several bunches on collimators or septum cannot be excluded in the present design.

Table 8 compares the melting temperature, the maximum temperature rise T_{max} expected in case of a single bunch impact, as well as the front temperature rise T_{front} of the dump, if hit by the full LHC beam without dilution, for different candidate materials. The only material for which both T_{max} and T_{front} are smaller than the melting temperature is carbon. Thus, carbon has been selected as the LHC dump material.[43]

Table 8. Candidate materials for the LHC beam dump.[43]

material	T_{melt} [°C]	T_{max} [°C/bunch]	T_{front} [°C/beam]
Be	1280	75	3520
C	4500	320	3520
Al	660	360	3390
Ti	1670	1800	3250
Fe	1540	2300	3120
Cu	1080	4000	2980

2.18 LHC Filling Pattern

The filling pattern of bunches around the machine determines the time structure of events seen by the experiments. The nominal LHC bunch spacing is 25 ns, and the total revolution time is 88.924 μs. The 25-ns spacing is interrupted by various gaps, which are needed for injection and extraction between the different injector storage rings and the LHC itself. A gap of 111 missing bunches is required for extraction from the LHC, gaps of 30 or 31 missing bunches correspond to the rise time of the LHC injection kickers, and various gaps of 8 missing bunches are related to the injection into the SPS.

The final nominal bunch pattern is complicated due to all these gaps. It can be expressed in mathematical notation as[44]

$$\begin{aligned}
(((72 \times b + 8 \times e) \times 3) &\quad + \quad 30 \times e) \times 2) \\
+((72 \times b + 8 \times e) \times 4) &\quad + \quad 31 \times e) \times 3) \\
+((72 \times b + 8 \times e) \times 3) &\quad + \quad 30 \times e) \times 3) \\
&\quad\quad +81 \times e),
\end{aligned}$$

where e refers to an empty place and b to a bunch.

Because of the many gaps different bunches in LHC experience different numbers of long-range collisions around the primary IPs. Even the number of head-on collisions in IP 2 and IP 8 is not the same for all the bunches. Indeed, less than half of the bunches are nominal ones, and all the others belong to one or another type of PACMAN bunch. This means that all these bunches will have different betatron tunes and different orbits.

According to the number and types of opposing bunches encountered, bunch equivalence classes can be defined.[44] Their number is almost comparable to the total number of bunches.[44]

Fortunately, careful analysis and simulations suggest that although different, the bunch orbits and tunes are still sufficiently similar that the lifetime and luminosity should not be much degraded.[45]

2.19 LHC Injectors

Before the beam is injected into the LHC it must be produced and accelerated in the injectors and pre-injectors.

These comprise, in order of decreasing energy, the Super Proton Synchrotron (SPS) the Proton Synchrotron (PS), and 4 PS Booster rings. In order to provide the high-quality beam demanded by the LHC a number of upgrades were necessary and new operational procedures and techniques of beam manipulation were introduced.

Historically, multiple bunches were generated in the PS by debunching (switching off the rf) and recapturing in a higher-harmonic rf system. A schematic of phase space evolution during slow debunching is shown in Fig. 23.

The problem with this scheme is that during the debunching process the microwave instability threshold is reached. Namely, while a bunch debunches, the density dN/ds and the local energy spread $\delta_{\rm rms}$ decrease by the same factor. The local instability threshold scales as

$$\left(\frac{dN}{ds}\right)_{\rm thr} \propto \delta_{\rm rms}^2, \tag{29}$$

which follows from the so-called Boussard criterion. Then, the beam becomes unstable as soon as its energy spread $\delta_{\rm rms}$ is small enough that this threshold condition is reached. The unwanted results are an unequal filling pattern and the non-reproducibility of the bunch intensities.

The new method developed for the LHC is a controlled bunch splitting without ever turning off the rf.[46] Instead, the relative amplitudes of various rf systems operating at different frequencies are varied as a function of time in such way that each bunch is

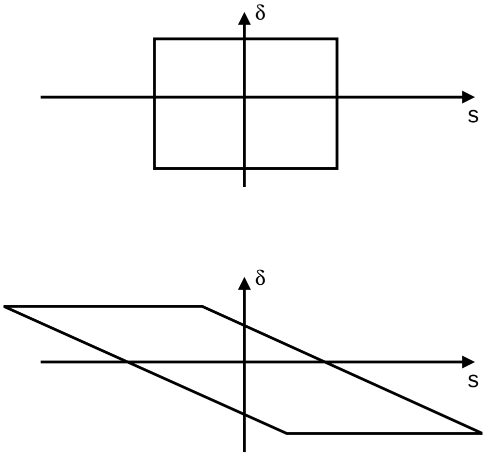

Fig. 23. Schematic of phase space evolution during slow debunching.

Table 9. Status of the PS for the LHC nominal beam.[47]

	achieved	nominal
protons per bunch	1.1×10^{11}	1.1×10^{10}
hor. emittance $\gamma\epsilon_x^{1\sigma}$ [μm]	2.5	3
vert. emittance $\gamma\epsilon_y^{1\sigma}$ [μm]	2.5	3
long. emittance $\epsilon_l^{2\sigma}$ [eVs]	0.35	0.35
total bunch length l_b [ns]	≤ 4	4
momentum spread $2\sigma_p/p$ [10^{-3}]	2.2	2.2

smoothly divided into 2 or 3 bunches. The nominal scheme for producing the LHC beam now starts with six high-intensity bunches injected into the PS. Each of these bunches is split into three, which is later followed by two further double splittings. The entire process thus transforms the original 6 into 72 bunches.

As an illustration, Fig. 24 shows a simulation of triple bunch splitting in the PS. The entire procedure has been successfully demonstrated experimentally, and since 2000 is routinely used to produce the LHC beam for machine studies in the SPS.

Table 9 demonstrates that the PS already delivers an LHC beam which meets all the design parameters.[47]

Work is also progressing in the SPS. In the winter shut down 2000/2001 a few thousand pumping ports were shielded in an attempt to reduce the longitudinal impedance.

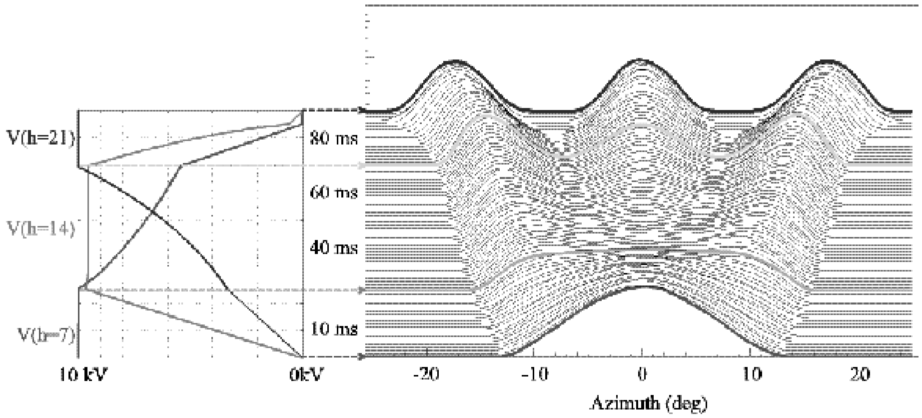

Fig. 24. Simulation of bunch splitting in the CERN PS in preparation for injection into the LHC.[46] The vertical axis is the time. The left picture shows the amplitudes of three rf systems operating at different frequencies (harmonic number h), which are used for this process. (Courtesy R. Garoby, 1999)

As a result of this effort, in 2001, bunch lengthening and strong impedance signals at 400 MHz are no longer observed.[48]

The evolution of the transverse impedance is also monitored by measurements of the coherent betatron tune shift with current and of the head-tail growth rates as a function of chromaticity.[49]

2.20 LHC as Heavy Ion Collider

Parameters for the LHC ion operation have been compared with the only existing ion collider, RHIC, in Table 1. The main limitation for ion operation varies with the ion mass.[6]

Heavy ion operation is limited by the electromagnetic processes occurring in the collision, namely by e^+e^- pair production and subsequent e^- capture.

The cross section of this process is about $\sigma_c \approx 100$ barn for Pb^{81+}-Pb^{81+} collisions, which corresponds to a rate of $\dot{N}_c \approx 10^5$ ions s^{-1} per side of IP at a luminosity of $L \approx 10^{27}$ $cm^{-2}s^{-1}$.

The cross section increases strongly with the atomic number $\sigma_c \propto Z^7$, whereas the energy deposition in a material only increases linearly with Z.

From the beam-optics point of view, for Pb ions a change in the ion charge by 1 unit is equivalent to a change in the relative momentum error of $\Delta\delta = 1.2\%$. Ions with a momentum error of this magnitude are lost in a region of about 1 m length at the entrance to the LHC arcs, where s.c. dipole magnets are located. The predicted loss rate for the nominal LHC ion parameters is close to the quench limit, thus setting a limit for the maximum luminosity.

Potential remedies might be a dynamic squeeze of the IP β function during the store, so as to optimize the integrated luminosity, or the installation of local collimators, which could reduce the loss rate in the magnets of the dispersion suppressor.

For light ions, the cross section for the above electromagnetic process is negligibe, and, for these ions, the main limitation for luminosity operation is the growth of the longitudinal emittance due to intrabeam scattering (IBS). For nominal parameters the IBS growth time is 10 hours. It scales as

$$\frac{1}{\tau_{\rm IBS}} \propto \frac{N_b Z^3}{A} \ , \tag{30}$$

where A is the ion mass in units of the proton mass. Taking into account the two limiting factors from above, the projected initial luminosities are 1.0×10^{27} cm^{-2}s^{-1} for Pb$^{82}_{208}$ ions, 6.6×10^{28} cm^{-2}s^{-1} for Kr$^{36}_{84}$ ions, and 3.1×10^{31} cm^{-2}s^{-1} for O$^{8}_{16}$ ions.

2.21 Electron Cloud

In 1999, the build up of an electron cloud was observed with the LHC beam in the SPS, and in 2000 also in the PS and in the PS-SPS transfer line.

Observations in the SPS are illustrated in Fig. 25, which shows beam loss in the last 4 bunches of a 72-bunch LHC batch, occuring about 5 ms after injection. The beam loss only occurs above the threshold current of multipacting, which manifests itself by a large vacuum pressure rise and by electron signals seen on dedicated electron-cloud monitors.

The electron cloud in the SPS is generated as follows. A small number of primary electrons is generated, *e.g.,* by gas ionization or beam loss. For the narrow LHC bunch spacing of 25 ns and typical vacuum-chamber half apertures of 2–3 cm, the number of electrons exponentially amplifies during the single passage of a 72-bunch train, by a process called beam-induced multipacting, already observed in the CERN ISR almost 30 years ago.[51]

In this section, we discuss build up, saturation, and decay of the electron cloud, then the wake fields and instabilities induced by the electrons, finally the heat load

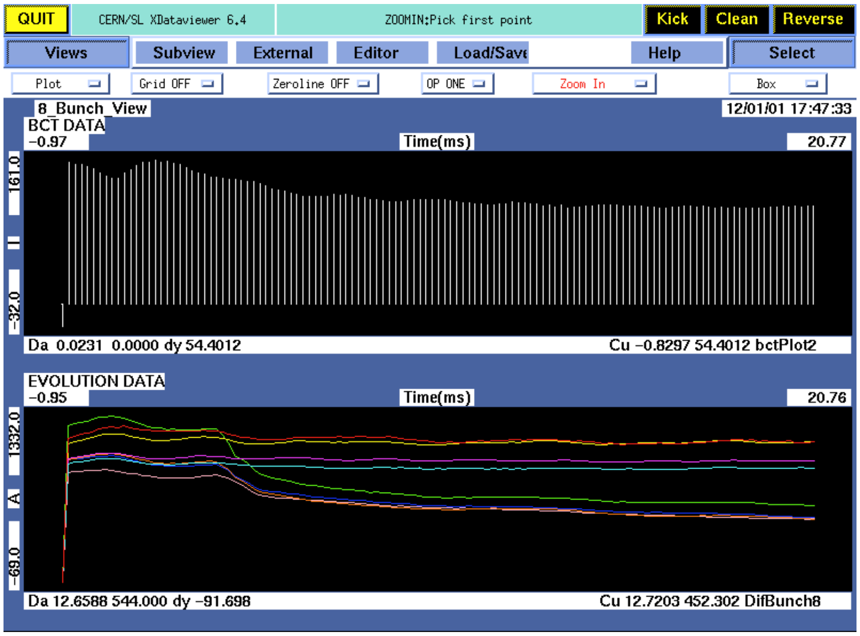

Fig. 25. Intensity of 72-bunch LHC beam in SPS vs. time. Batch intensity (top) and bunch intensity for the first 4 bunches and the last 4 bunches (where losses are visible after about 5 ms) of the batch (bottom).[50] (Courtesy G. Arduini, 2001)

from the electrons, which is the largest concern for the LHC, and the presently foreseen countermeasures.

We use the variable λ to denote the electron line density; t is the time and s the position along the beam line. For a beam current of 0.5–1 A, the processes contributing to the generation of electrons are (1) residual gas ionization, with a typical rate of $d^2\lambda_e/(ds\ dt) \approx 5 \times 10^{11}$ e$^-$ m^{-1}s^{-1}; (2) synchrotron radiation and photo-emission, with a typical rate $d^2\lambda_e/(ds\ dt) \approx 5 \times 10^{18}$ e$^-$ m^{-1}s^{-1}; and (3) secondary emission, consisting of true secondaries and also of elastically reflected or rediffused electrons. If the average secondary emission yield is larger than 1, the secondary emission leads to an exponential growth.

Indeed, the key process of the electron-cloud formation in the LHC is the secondary emission, and the most important parameter the secondary emission yield. The latter depends on the energy of the primary electron. A parametrization for the LHC vacuum chamber[52] is shown in Fig. 26. The secondary electrons consist of two components. The true secondaries are emitted at low energies, of the order of a few eV. Their yield reaches a maximum value $\delta_{\max}$ at a certain impact energy $\epsilon_{\max}$, and the yield curve is well approximated by a universal function with only these two free parameters. A certain fraction of the incident electrons is elastically reflected. The lower the energy of the incident electron, the larger is the proportion of the reflected electrons. These reflected electrons are responsible for the fact that the total secondary emission yield does not approach zero if the energy of the primaries approaches zero, but remains at a finite value. The contribution from elastically reflected electrons to the total yield is also illustrated in Fig. 26. The nonzero yield value for low energies implies that a certain number of low-energetic electrons will survive for a long time inside the vacuum chamber, even if there is a large gap in the bunch train.

The build up of the electron cloud due to beam-induced multipacting does not continue indefinitely, but it saturates, roughly at the moment when the average number of electrons per unit length is equal to the average line density of beam protons or positrons. In other words, the order of magnitude of the saturated electron line density can be estimated as

$$\lambda_{\rm sat} \approx \frac{N_b}{L_{\rm sep}}, \tag{31}$$

where N_b is the bunch population, and $L_{\rm sep}$ the bunch spacing. The corresponding volume density is obtained by dividing with the beam-pipe cross section.

In the SPS the small number of primary electrons produced via gas ionization is

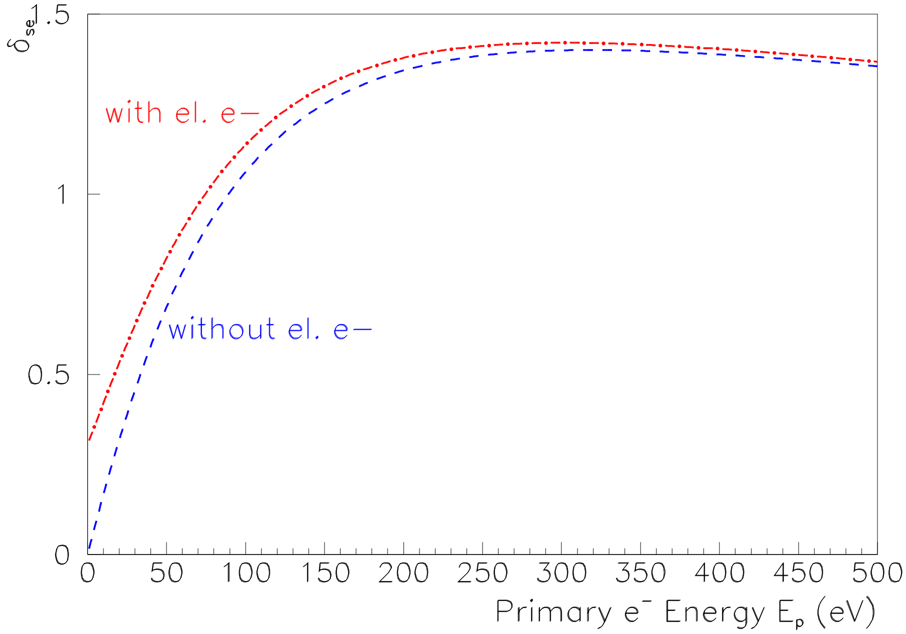

Fig. 26. Secondary emission yield for perpendicular incidence vs. the primary electron energy with and without elastically scattered electrons. The parametrization is based on measurements for copper surfaces.[52]

amplified by multipacting so strongly that saturation is reached already after about 30 bunches. In the LHC the number of primary photoelectrons will be much larger than that of ionization electrons in the SPS. Figure 27 shows a schematic of the electron-cloud build up in the LHC beam pipe.

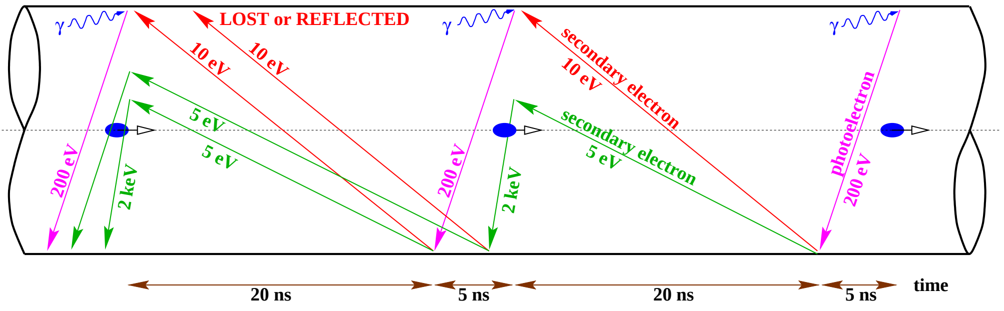

Fig. 27. Schematic of electron-cloud build up in the LHC beam pipe. (Courtesy F. Ruggiero)

The condition for proper multipacting is[53]

$$n_{\min} \equiv \frac{h_y^2}{N_b r_e L_{\text{sep}}} = 1, \tag{32}$$

which describes the situation that the travel time of electrons across the chamber exactly equals the time between two bunches, and includes the assumption that the electrons are close to the chamber wall when the bunch arrives. However, it should be noted that the condition (32) is neither necessary nor sufficient to observe electron amplification. If the parameter $n_{\min}$ is smaller than one, low-energetic secondary electrons are produced before the next bunch arrives. They will move slowly through the chamber and are accelerated only when a bunch passes by. On the other hand, if $n_{\min}$ is larger than 1, an electron will interact with more than 1 bunch. In either situation electron amplification can still occur. This is illustrated in Table 10 which lists parameters for several accelerators where electron clouds have been observed or are predicted to occur. The values of $n_{\min}$ are also listed for each ring. They extend over several orders of magnitudes.

Thus $n_{\min}$ is not a reliable parameter to assess the possibility of multipacting. In order to predict the occurrence and magnitude of multipacting, detailed computer simulations are required. Figure 28 illustrates the ingredients of such simulations.[55] Both bunches and interbunch gaps are split into slices. For each slice, the motion of elec-

Table 10. Comparison of parameters related to the electron-cloud build up for the LHC beam in the CERN PS, SPS, and the LHC with those of several other proton and positron storage rings, in which an electron cloud is observed or expected.[54]

accelerator	PEP-II	KEKB	PS	SPS	LHC	PSR	SNS
species	e^+	e^+	p	p	p	p	p
population N_b [10^{10}]	10	3.3	10	10	10	5000	10000
spacing $L_{\rm sep}$ [m]	2.5	2.4	7.5	7.5	7.5	(108)	(248)
bunch length σ_z [m]	0.013	0.004	0.3	0.3	0.077	25	30
h. beam size σ_x [mm]	1.4	0.42	2.4	3	0.3	25	0.6
v. beam size σ_y [mm]	0.2	0.06	1.3	2.3	0.3	7.5	0.6
ch. $\frac{1}{2}$ size h_x [mm]	25	47	70	70	22	50	100
ch. $\frac{1}{2}$ size h_y [mm]	25	47	35	22.5	18	50	100
synchrotron tune Q_s	0.03	0.015	0.004	0.006	0.002	0.0004	0.0007
circumf. C [km]	2.2	3.0	0.63	6.9	27	0.09	0.22
beta function β	18	15	15	40	80	5	6
parameter $n_{\rm min}$	1	10	0.58	0.24	0.15	0.0002	0.0001

trons is computed under the influence of the beam field, external magnetic fields, electron space-charge field, and the image forces induced by both beam and electrons. For each passing bunch slice, a certain number of primary electrons is created. Whenever an electron is lost to the wall, its charge state is changed according to the secondary emission yield computed for its energy and impact angle, and the electron is re-emitted representing either a true secondary or an elastically scattered electron.

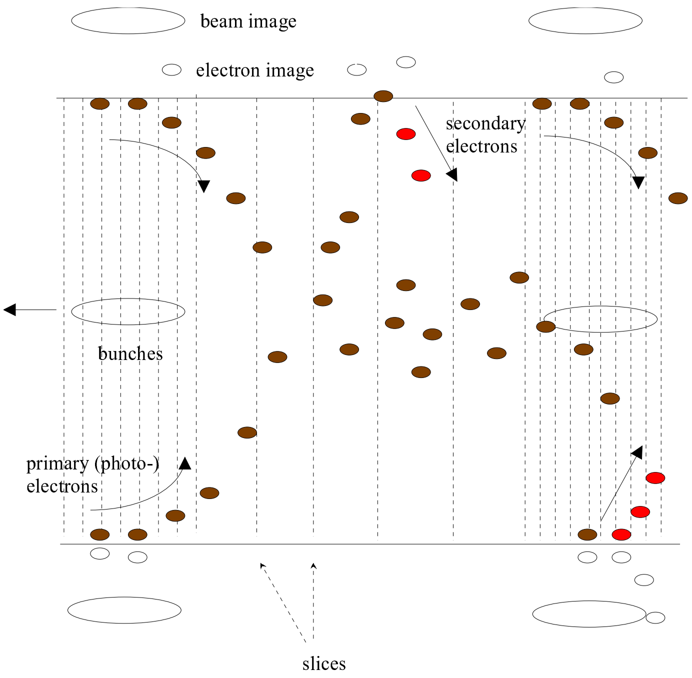

Fig. 28. Schematic illustrating various ingredients of the electron-cloud simulations.

In the actual accelerator, various indicators can signal the electron-cloud build up, such as (1) a nonlinear pressure rise with beam current, (2) current data from electrostatic pick ups or dedicated electron monitors, (3) the measured tune shift along the train, (4) the beam-size blow up along the train, and where applicable, (5) a drop in luminosity. All these items entail direct informations about the electron density.

As an example, we mention two estimates of the electron-cloud density in the SPS. The first is based on the pressure rise, and is due to O. Gröbner.[56] The equation for the pressure balance reads

$$S_{\rm eff} P/(k_B T) = Q \tag{33}$$

where $S_{\rm eff}$ denotes the pumping speed in volume per meter per second, $Q = \alpha d\dot{\lambda}_{t,e}/ds$ the total flux of molecules per unit length (α is the desorption yield per electron, and

$\lambda_{t,e}$ the number of electrons hittng the chamber wall per unit length and per bunch train passage) and $P = k_B TN/V$, where N/V is the number of gas molecules per unit volume, and P the pressure. We insert the expression for Q into Eq. (33), and solve for $d\lambda_{t,e}/ds \approx T_{\rm rev}(d\dot{\lambda}_{t,e}/ds)$

$$\frac{d\lambda_e}{ds} \approx \frac{T_{rev}}{\alpha k_B T}\, S_{\rm eff} P, \tag{34}$$

where $T_{\rm rev}$ is the revolution period.

With an enhanced pressure of $P = 100$ nTorr, $\alpha \approx 0.1$ and $S_{\rm eff} \approx 20\,{\rm l\,s^{-1}\,m^{-1}}$ one estimates

$$\frac{d\lambda_e}{ds} \approx 10^{10} \frac{\rm electrons}{\rm bunch-train\ meter}\ . \tag{35}$$

The second estimate is directly related to the signal seen on the transverse damper pick up in the SPS, which indicates that a few 10^8 electrons per bunch passage are deposited on the pick-up.[57] This number amounts to $10^9 - 10^{10}$ per train, or, for an effective pick-up length of about 10 cm, to[57]

$$\frac{d\lambda_e}{ds} \approx 10^{10} \frac{\rm electrons}{\rm bunch-train\ meter}\ . \tag{36}$$

The two estimates, (35) and (36), are consistent.

Figure 29 shows two difference signals measured between the plates of two identical electro-static pick ups in the SPS. Without perturbation from the electron cloud, the difference signal should be proportional to the beam offset in the chamber. One of the two signals in Fig. 29 is processed at low frequencies, the other in a higher frequency band around 120 MHz. The shift in the baseline of the low-frequency signal, which is seen near the center of the 1.8-μs bunch train and persists in the 20-μs gap without beam, indicates a net charge transfer between the pick-up plates, due to the multipacting electrons. The same distortion is not visible in the high-frequency signal, which may suggest that the frequency spectrum of the electron cloud current between the plates of the pick up does not extend up to 120 MHz.

Figure 30 displays a simulation of the electron-cloud build up for the SPS parameters. The simulation can reproduce the observed saturation of the electron-cloud build up at the center of the bunch train, provided that the elastically reflected electrons are included in addition to the true secondaries.

In the SPS also a positive tune shift is observed which starts between the 10th and 20th bunch of the train and is of order $\Delta Q \approx 0.01$. The tune shift permits an independent estimate of the electron density, which is consistent with the other two estimates from above.

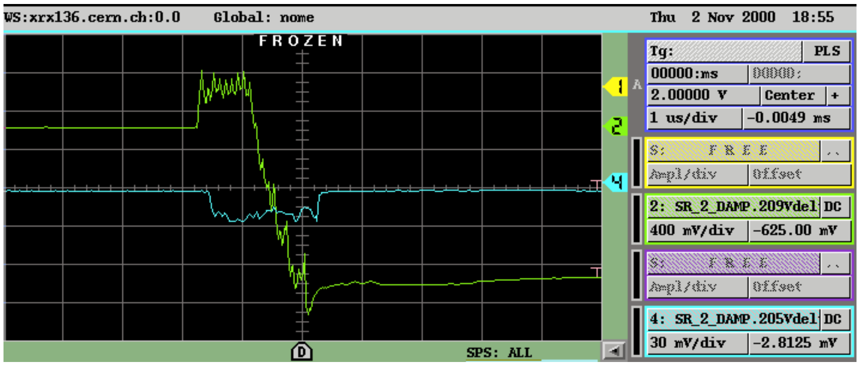

Tg:
00000:ms 00000:
2.00000 V
1 us/div -0.0049 ms
S: F R E E
Ampl/div Offset
2: SR_2_DAMP.209Vdel DC
400 mV/div -625.00 mV
S: F R E E
Ampl/div Offset
4: SR_2_DAMP.205Vdel DC
30 mV/div -2.8125 mV

Fig. 29. Difference signals on damper pick-up during the passage of an LHC batch in the SPS (1μs/div); the signal observed at low frequency (green line, shifted due to electron cloud) and the downmixed signal sampled at 120 MHz (blue line, without final offset). (Courtesy W. Hofle, 2000)

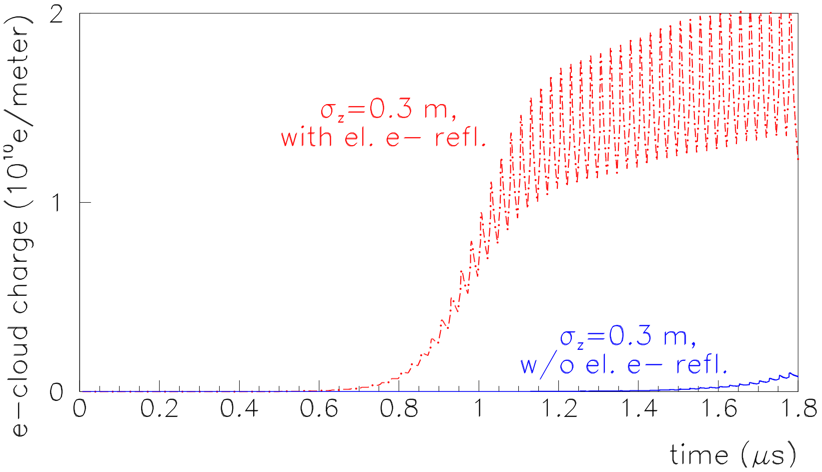

Fig. 30. Simulated evolution of the electron line density in units of 10^{10} m^{-1} as a function of time in s, for an SPS dipole chamber, with and without elastic electron reflection.[55]

The electron cloud, once generated, can gives rise to wake fields and instability. Namely, the electrons couple the motion of subsequent bunches and can thereby couple the motion of successive bunches. They also introduce coherent and incoherent tune shifts. However, in the SPS the most harmful effect is a single-bunch instability, which presumably is of a similar nature as those observed in the positron rings of the PEP-II and KEKB B factories. This instability appears to be the analogue of the strong head-tail instability caused by a conventional wake field. (The strong head-tail instability is also called the transverse-mode coupling instability, abbreviated as TMCI.) In addition, the electron cloud might excite the regular head-tail instability, and also induce longitudinal electric fields, albeit recent analysis suggests that the latter two effects are small.

We limit the following discussion to the TMCI-like instability. Several dedicated computer programmes were written, at KEK and CERN, which model this instability. In the simulation both the electrons and a bunch of the beam are represented by macroparticles. On each turn the bunch interacts with a fresh uniform cloud of electrons, assumed to be generated by the preceding bunches. The electron cloud can act like a wake field and enhance an initial head-tail perturbation in the beam.

During the bunch passage, the electrons oscillate in the beam potential. Figure 31 shows a snapshot of the simulated electron phase space at the end of a bunch passage.

If the electrons perform several transverse oscillations over the length of the bunch, they may be adiabatically trapped in the beam potential and remain at the center of the chamber for a long time.[59]

Using the WKB approximation the adiabaticity condition for this trapping process can be written as

$$A \equiv \sigma_z \omega_{e,y} \sqrt{8e}/c \gg 1 \ , \tag{37}$$

where $\omega_{e,y}$ is the vertical electron angular oscillation freqency, and $e = 2.718\ldots$ Inserting the accelerator parameters into Eq. (37), we obtain $A \approx 10$ for KEKB, PEP-II, PS, SPS, and LHC. Hence, in all these accelerators, electrons may be trapped.

If simulations are performed with the electron cloud as the only perturbation, the beam size increases smoothly but signficantly with time. If the position-dependent tune shift due to the proton space-charge force in the SPS at 26 GeV/c is also included, the simulated instability becomes more violent.[60] This is illustrated in Fig. 32.

Figure 33 compares the simulated emitance growth in both transverse planes, computed using two different models of the beam field, namely a soft-Gaussian approximation and a particle-in-cell (PIC) code.[61] The two results are comparable. Either

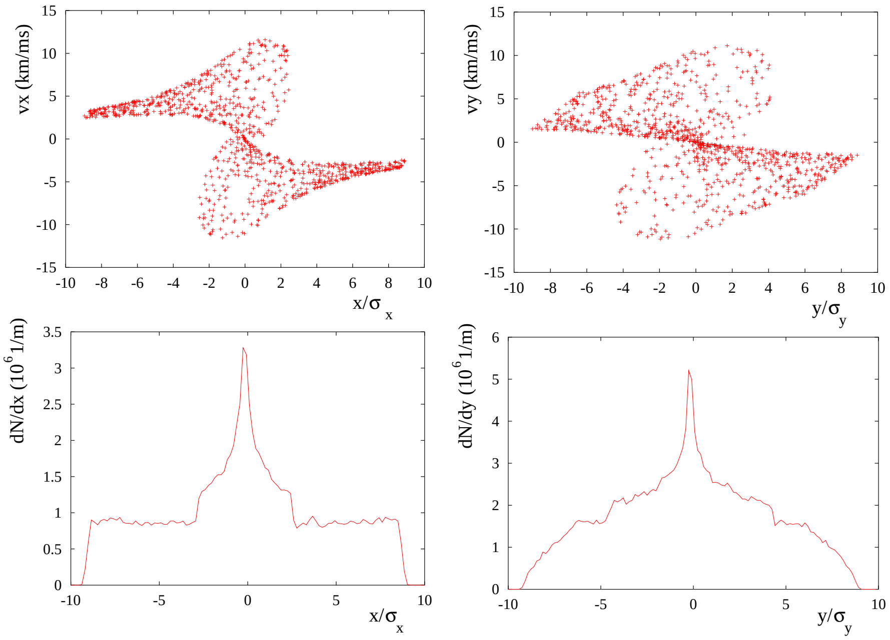

Fig. 31. Snapshots of the horizontal and vertical electron phase space (top) and their projections onto the position axes (bottom).[58] (Courtesy G. Rumolo, 2001)

simulation predicts a rapid emittance growth within a few ms, which is consistent with the time scale of the observed beam loss.

The effective transverse wake field of the electron cloud can be obtained from the simulation, by displacing a slice of the bunch transversely, and computing the resulting force on the subsequent bunch slices. A typical result is shown in Fig. 34. Because of the electron accumulation inside the bunch during its passage and due to the nonlinearities of the forces acting between beam and electrons, the computed wake fields depend on the position of the displaced slice, as illustrated in this example.

Either using a two-particle model,[62] or approximating the simulated wake field by a broadband resonator,[63] one can estimate the TMCI threshold. Table 11 compares the estimated threshold cloud density with the expected saturation density for various accelerators. The table demonstrates that almost all the accelerators listed may operate above the electron-cloud instability threshold.

At the SPS direct evidence for the head-tail instability comes from a wideband pickup which measures the transverse position every 0.5 ns, compared with a total bunch length of 4 ns. In the vertical plane, significant motion is detected inside the bunch. The oscillations of subsequent bunches are uncorrelated. The wave length of

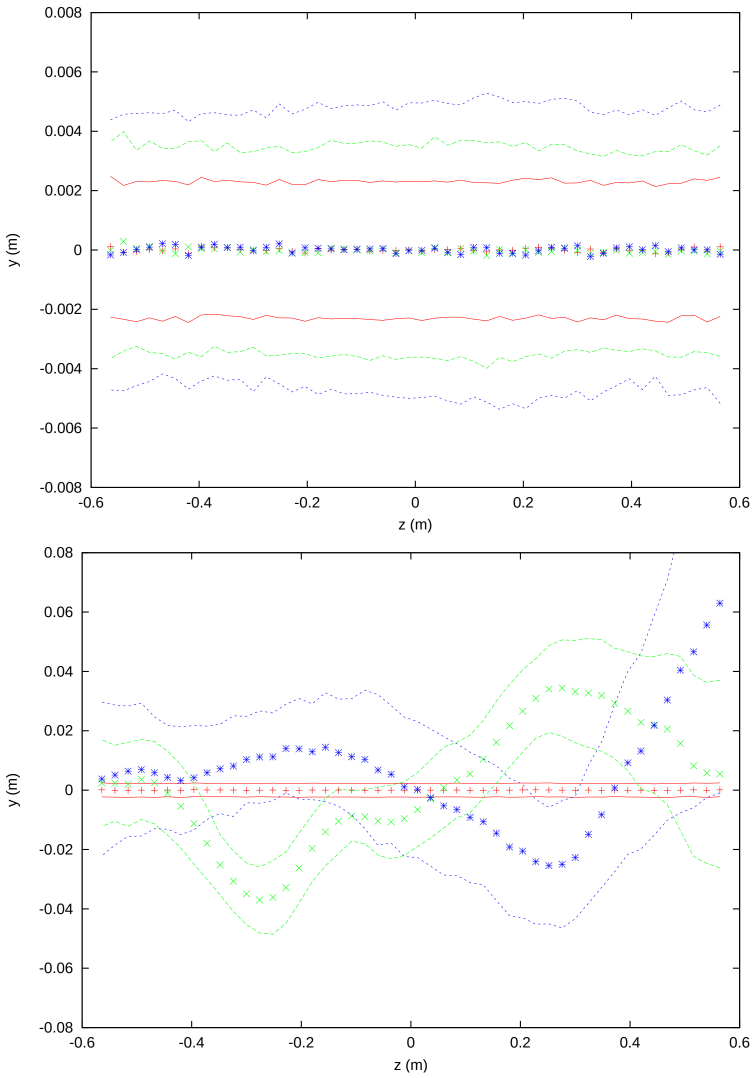

Fig. 32. Simulated bunch shape after 0, 250 and 500 turns (centroid and rms beam size shown) in the CERN SPS with an e$^-$ cloud density of $\rho_e = 10^{12}$ m^{-3}, without (top) and with (bottom) proton space charge.[60] (Courtesy G. Rumolo, 2001)

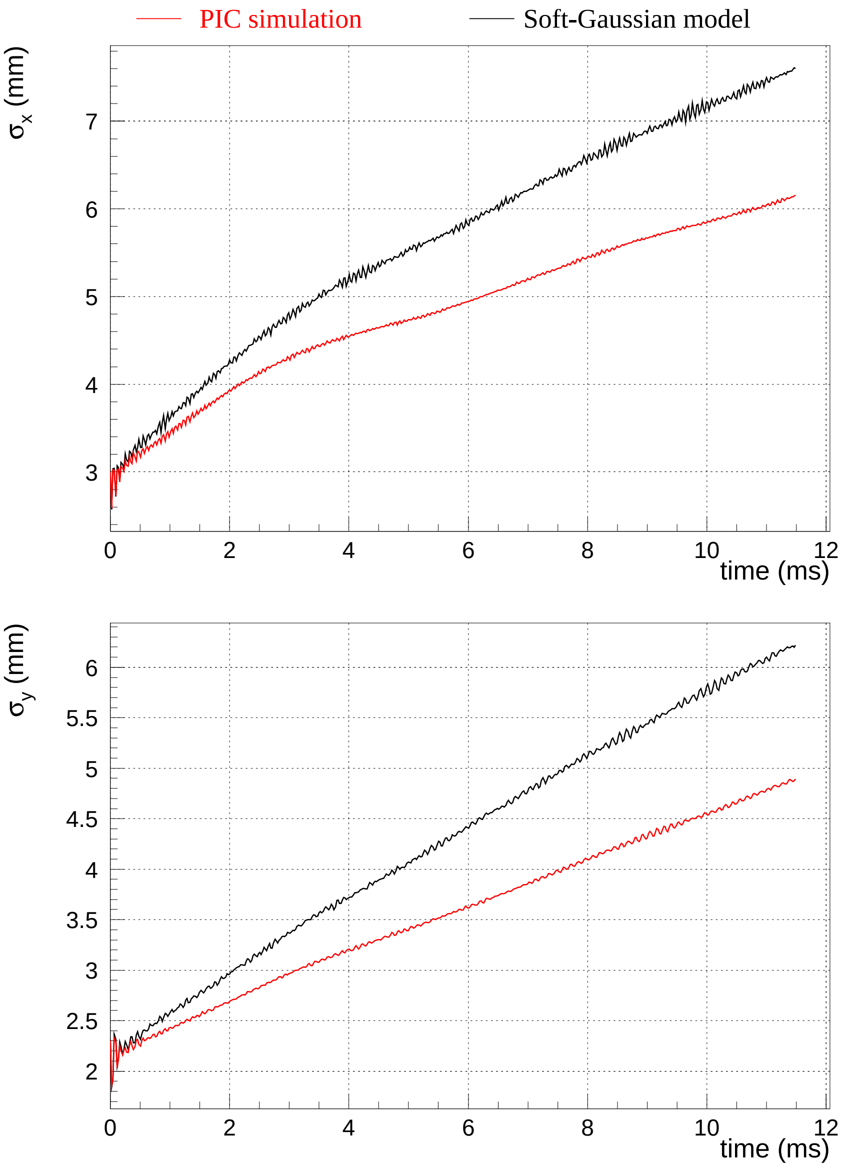

Fig. 33. Beam size evolution for an SPS bunch interacting with an electron cloud as predicted by different simulation approaches,[61] for a cloud density of $\rho_e = 10^{12}$ m^{-3}. (Courtesy G. Rumolo, 2001)

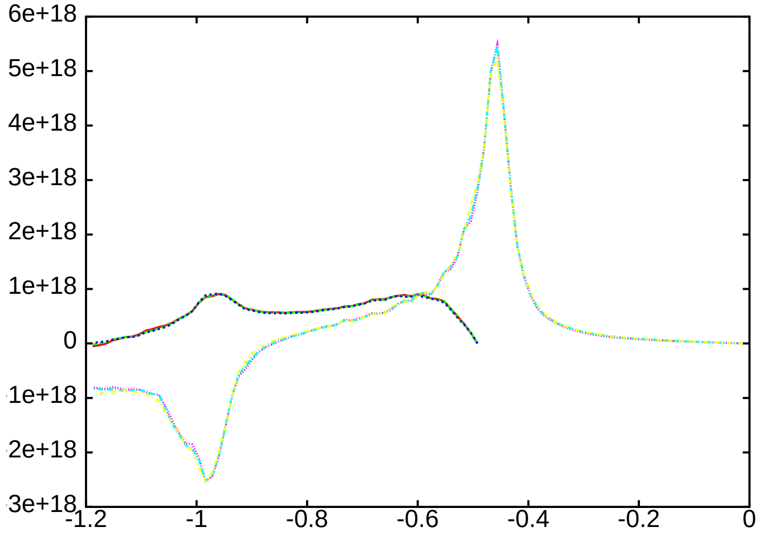

Fig. 34. Simulated wake force in V/m/C computed by displacing slice 1 and 40 (out of 100) of a Gaussian bunch with rms length 0.3 m, as a function of longitudinal position along the bunch in units of meter. The bunch center is at -0.6 m and the bunch head on the right.[58] (Courtesy G. Rumolo, 2001)

Table 11. The number of electron oscillations during a bunch passage, the estimated electron-cloud TMCI threshold, and the ratio of electron equilibrium density to threshold density, for various accelerators.[54]

accelerator	PEP-II	KEKB	PS	SPS	LHC	PSR	SNS
e^- osc./bunch $n_{\rm osc} \equiv \omega_e \sigma_z/(\pi c)$	0.8	1.0	1	0.75	3	34	970
TMCI threshold ρ_e [10^{12} m^{-3}]	1	0.5	5	0.25	3	(0.6)	(0.5)
density ratio $\rho_{e,\rm sat}/\rho_{e,\rm thresh}$	19	4	0.35	11	4	(92)	(27)

the wake field was fitted from the data by K. Cornelis, and it agrees with the calculated wavelength of electron oscillations.[64]

Simulations including both the electron cloud and, in addition, a regular broadband impedance show that the instability can be suppressed by a large positive chromaticity,[65] in accordance with observations.

The heat deposited by electrons on the beam screen is a major concern for the LHC. Simulated electron impact energies extend up to several 100s of eV. This is much larger than the typical emission energy of secondaries of only a few eV. In other words, the electron cloud extracts a significant energy from the beam, and transfers it to the chamber wall.

The importance of this issue for the LHC is illustrated in Fig. 35, which shows the simulated arc heat load, averaged over dipoles, field-free regions and quadrupoles, as a function of bunch population for various values of the maximum secondary emission yield $\delta_{\rm max}$. Also indicated is the maximum cooling capacity available for the electron cloud. The figure demonstrates that in order to reach the design bunch intensity of $N_b = 1.1 \times 10^{11}$ the secondary emission yield must not be much larger than 1.1.

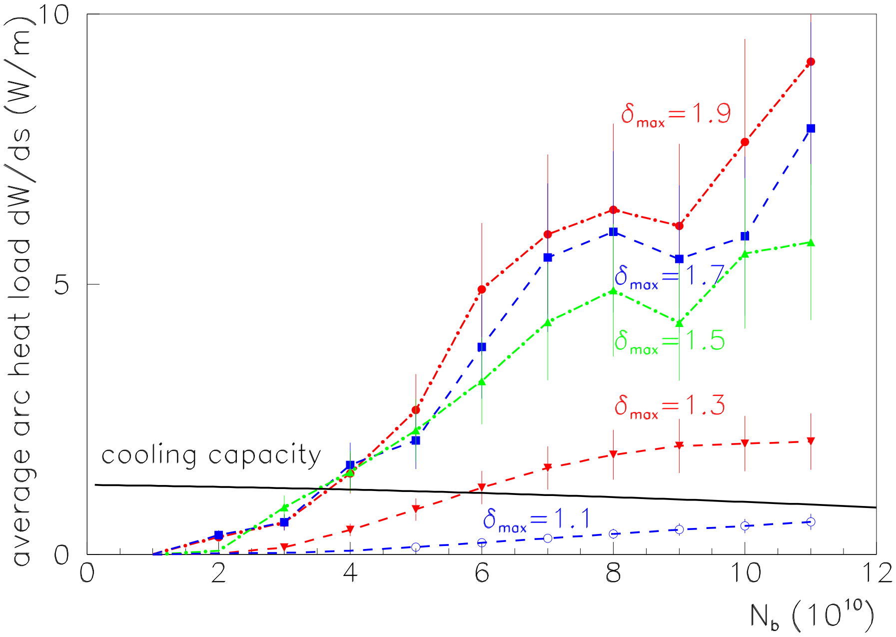

Fig. 35. Average arc heat load and cooling capacity as a function of bunch population N_b, for various values of the maximum secondary emission yield $\delta_{\rm max}$.

Figure 36 shows the electron distribution simulated for an LHC dipole. The vertical stripes with enhanced electron density correspond to the regions with maximum multipacting. If such electron stripes would lie on top of the beam-screen pumping slots, electrons could pass directly to the 1.9-K cold bore, instead of being absorbed by the beam screen. The cooling capacity for the cold bore is much smaller, and a quench would be a likely consequence.

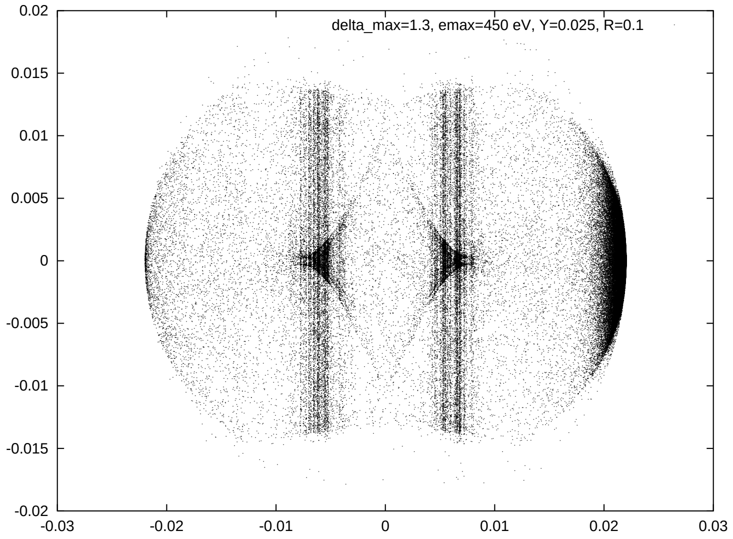

Fig. 36. Snapshot of the transverse electron distribution in an LHC dipole chamber, for a maximum secondary emission yield of $\delta_{\mathrm{max}} = 1.3$.[66]

Three main countermeasures against the electron cloud are foreseen, *i.e.*,

- to install a 'sawtooth chamber' (with a height of about 35 μm and a period of 200 μm), which reduces the photon reflection in the arc dipoles;
- to coat all warm sections with a getter material TiZr, that exhibits a low secondary emission yield;
- and to rely on surface conditioning during the commissioning, which should reduce the maximum secondary emission yield to a value of 1.1; an electron dose of about 10 C/mm^2 is needed to reach this target value.[67]

In 2001 several novel electron cloud detectors were installed in the SPS by G. Arduini, J.M. Jimenez, et al., whose purpose is to serve as a benchmark for the simulation and to directly provide measurements under conditions very similar to those in the LHC.

The newly installed SPS electron-cloud detectors include[68]: (1) pick-ups which measure the electron characteristics, in particular, the e^- cloud build up and the e^- energy distribution; they also allow for triggering on the batch; (2) monitors which characterize the behavior of the electrons in a dipole magnetic field; 2 different designs were developed for this purpose, the first is a 'strip detector', the second a so-called 'triangle detector'; (3) an in-situ measurement of secondary emission yield, which can verify the effect of surface processing; (4) ion detectors to exclude ion-stimulated desorption as a source of the pressure rise; and (5) a so-called WAM_PAC Cu calorimeter which directly measures the heat load from the electron cloud.

First observations with these detectors are promising. The strip monitor clearly reveals the horizontal position and width of the multipacting electrons. Above a bunch intensity of $N_b \approx 5 \times 10^{10}$ protons, the single strip splits into two, which for further increasing bunch current move towards the outside of the chamber. This behavior agrees well with the simulations. Preliminary measurements using a biasing grid and the triangular detector suggest average electron energies of the order of 75 eV. The calorimeter measures a power deposition, which, scaled to the LHC, might correspond to a heat load of the order of 1 W/m, comparable to typical predictions.

The in-situ change in the secondary emission yield was also measured. After about 24-hours of effective conditioning time with an LHC beam, the maximum secondary emission yield $\delta_{\max}$ had decreased from 2.3 to 1.8, which demonstrates that surface scrubbing is acting as foreseen.

3 Beyond LHC: LHC-II and VLHC

Once the LHC is operating, the particle physicists will push for higher luminosity and higher energy. A feasibility study for an 'LHC-II' has been launched at CERN.[69]

The LHC luminosity can be raised by increasing the number of bunches, which might imply a larger crossing angle. As a next step, one might contemplate more exotic schemes, where, *e.g.*, 'crab' cavities on either side of the collision point deflect the head and tail of the bunches transversely in opposite directions such that the bunches collide effectively head on.

The availability of stronger or cheaper magnets will facilitate the path towards higher energy and indicate the direction to follow.

Synchrotron radiation and emittance control will become an important issue, as the higher-energy machines will operate in a new regime, where the effects of synchrotron

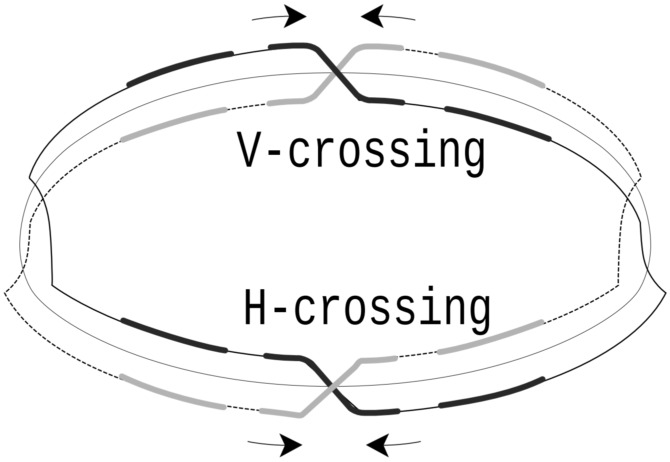

Fig. 37. Schematic of Super Bunches in a High-Luminosity Collider.[71]

radiation become more and more noticable, and where the radiation equilibrium emittance is much smaller than the injected emittance. The shrinking of the emittance during the store could be a nuisance, since the beam-beam tune shift increases with time and the beam-beam limit may be reached soon after injection, potentially leading to an unstable situation. On the other hand, intrabeam scattering is still significant for these energies and emittances, and may balance the radiation damping. Thus, a careful study of emittance control is clearly an important topic for the future hadron machines.[70]

Some collective effects can also prove more severe. If the circumference is large, the coupled-bunch resistive wall instability may require several local feedbacks. More worriesome still is the electron cloud, which might introduce an ultimate limitation.

Also the debris from the IP, the quench limits and the question of a safe beam abort will be major challenges.

Lastly, there is an option to collide continuous beams as in the ISR. In reality these would be rather 'quasi-continuous beams' or 'superbunches', occupying only a small fraction of the total circumference and being confined by barrier rf buckets,[71] as illustrated in Fig. 37. The barrier buckets may be generated by induction acceleration modules.[71]

Such continuous beams or superbunches are based on the successful experience of the ISR and hold various promises:

- in conjunction with alternating crossing at two IPs superbunches can provide a higher luminosity with acceptable beam-beam tune shift;
- PACMAN bunches are absent and the beam particles almost identical to one an-

other, each sampling all longitudinal positions with respect to the opposing beam;

- the electron-cloud build up should be strongly suppressed, since electrons cannot gain any energy in the constant beam potential;
- superbunches might allow for stochastic cooling, which is not an option for bunched beams.[72]

A primary reason why coasting beams were abandoned, despite of the ISR success, was the scarcity of antiprotons. This is no longer a problem for proton-proton colliders.

A large number of questions need to be answered, however, before a superbunch scheme could be envisioned for a future LHC upgrade. Ongoing work at CERN includes the optimization of the beam parameters, such as length, line density, and total number of superbunches, which would maximize the luminosity, while maintaining a tolerable beam-beam tune shift and an acceptable heat load, and obeying the timing constraints imposed by the (induction) rf system, the capacity of the injectors, the filling time, and the beam abort system.

3.1 Prospects for Luminosity and Beam-Beam Tune Shifts

Considering round beams, *i.e.*, $\beta_x^* = \beta_y^*$ and $\epsilon_x \approx \epsilon_y$, and including the hourglass effect and a horizontal crossing angle θ_c, the luminosity for both normal and superbunches can be expressed as

$$L = \frac{f_{\rm coll}\lambda_1\lambda_2\beta^*}{2\pi\sigma_0^2}\int_{-l_{\rm det}/(2\beta^*)}^{l_{\rm det}/(2\beta^*)} \frac{1}{1+u^2}\;\exp\left[-\frac{{\beta^*}^2\theta_c^2/\sigma_0^2}{4}\,\frac{u^2}{1+u^2}\right]\; f(u)\,du \tag{38}$$

where

$$f(u) = l_{\rm bunch} \tag{39}$$

for a superbunch whose length $l_{\rm bunch}$ is much larger than the effective length of the detector $l_{\rm det}$, and

$$f(u) = \sqrt{\pi}\sigma_z \exp\left[-\frac{{\beta^*}^2 u^2}{\sigma_z^2}\right]. \tag{40}$$

for a regular Gaussian bunch of rms length σ_z. The coefficients λ_1 and λ_2 denote, for a normal bunch, the maximum line density $\lambda = N_b/(\sqrt{2\pi}\sigma_z)$, and, for a superbunch, the constant line density $\lambda = N_b/l_{\rm bunch}$.

Considering a single collision point with horizontal crossing, the maximum beam-beam tune shifts, experienced by a particle at the center of the bunch, are

$$\Delta Q_x \;=\; -\frac{\lambda r_p}{\pi\gamma}\int_{-l/2}^{l/2}\left(\beta^* + \frac{s^2}{\beta^*}\right)\left[\left(\frac{1}{(\beta^*+s^2/\beta^*)\,\epsilon} + \frac{1}{\theta_c^2 s^2}\right)\right.$$

$$\exp\left(-\frac{\theta_c^2 s^2}{2\left(\beta^* + s^2/\beta^*\right)\epsilon}\right) - \frac{1}{\theta_c^2 s^2}\Bigg] \; g(s)\, ds$$

$$\Delta Q_y \;=\; -\frac{\lambda r_p}{\pi\gamma}\int_{-l/2}^{l/2}\left(\beta^* + \frac{s^2}{\beta^*}\right)\left[\frac{1}{\theta_c^2 s^2}\,(1- \exp\left(-\frac{\theta_c^2 s^2}{2\left(\beta^* + s^2/\beta^*\right)\epsilon}\right))\right] \; g(s)\, ds \;, \tag{41}$$

where

$$g(s) = \exp\left(-2\frac{s^2}{\sigma_z^2}\right) \tag{42}$$

for a regular bunch, and $g(s) = 1$ for a superbunch, and λ is the (maximum) line density of the opposing, equal to either λ_1 or λ_2 in the luminosity formula. Here, the electrostatic interaction between the two bunches is assumed to occur between $-l/2$ and $l/2$. Outside of this range the beams are either separated by a bending magnet, or shielded from each other. The distance l can be much larger than the effective detector length $l_{\rm det}$.

Figure 38 shows the luminosity and beam-beam the shifts as a function of crossing angle as computed from Eqs. (38) and (41) for the so-called ultimate LHC bunch intensity of $N_b \approx 1.7 \times 10^{11}$ with regular Gaussian bunches of 7.7-cm rms length, and considering collision-point beta functions which are reduced from the nominal value of 0.5 m to 0.25 m. The number of bunches is unchanged compared with the nominal scenario. Assuming two interaction points with alternating crossing, the maximum total beam-beam tune shift is given by the sum $\Delta Q_{\rm tot} = (\Delta Q_x + \Delta Q_y)$. This total tune shift is also shown in the figure. For crossing angles of 300–400 μrad, it is quite moderate, and much below the highest values achieved elsewhere (compare Table 5).

Figure 39 shows the corresponding curves for a coasting beam or for a superbunch scheme. If the entire ring is filled, with 40 A dc current, the luminosity is of the order of 5×10^{36} cm^{-2}s^{-1}. If only a 1/40th of the ring is occupied the luminosity could still 10^{35} cm^{-2}s^{-1} with an average current of 1 A. These parameters have not yet been fully optimized.

3.2 Crab Cavities

As shown in Fig. 38 the luminosity decreases for larger crossing angles. This luminosity loss can be avoided by means of ‘crab crossing’, a scheme which was first proposed for linear colliders,[73] and will be tested at the KEK B factory. The basic idea of crab

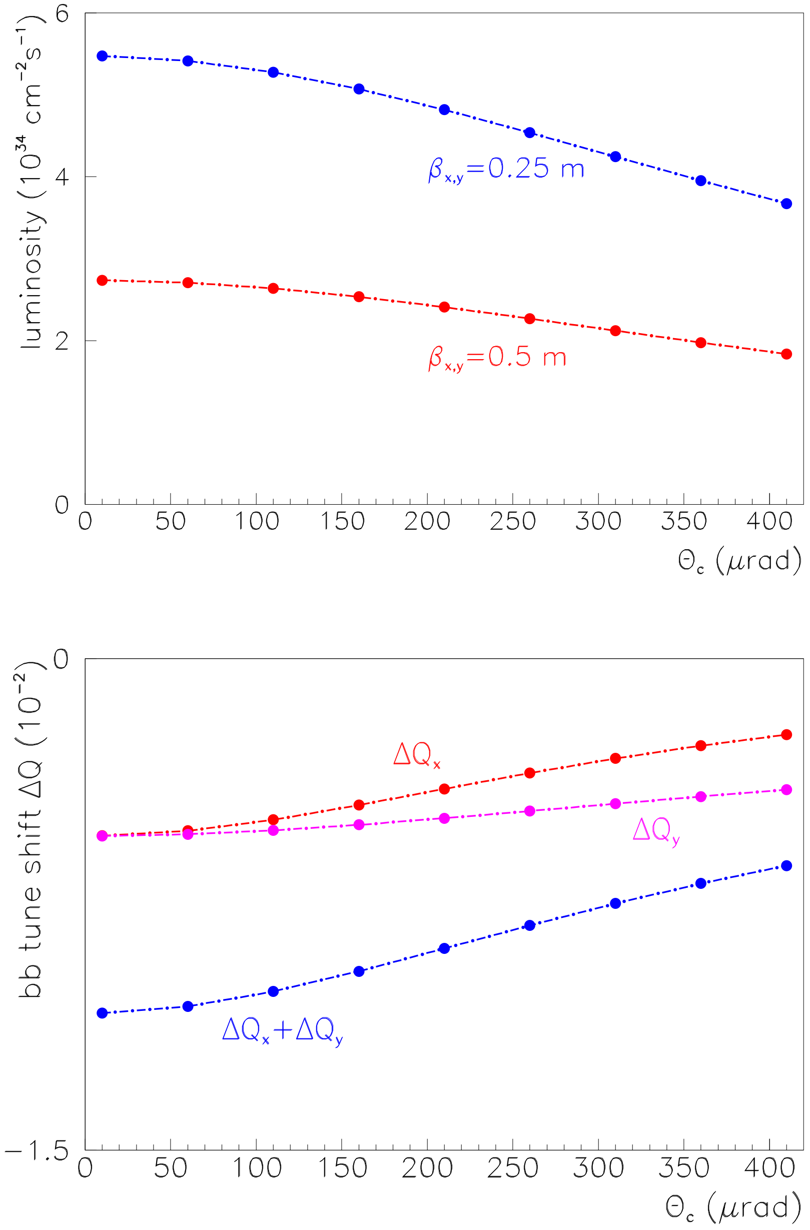

Fig. 38. Luminosity (top) and total beam-beam tune shift (bottom) vs. crossing angle; parameters: $N_b = 1.7 \times 10^{11}$, $\beta^* = 0.25$ m, $\sigma_z = 7.7$ cm, $n_b = 2800$, $\gamma\epsilon_\perp = 3.75$ μm.

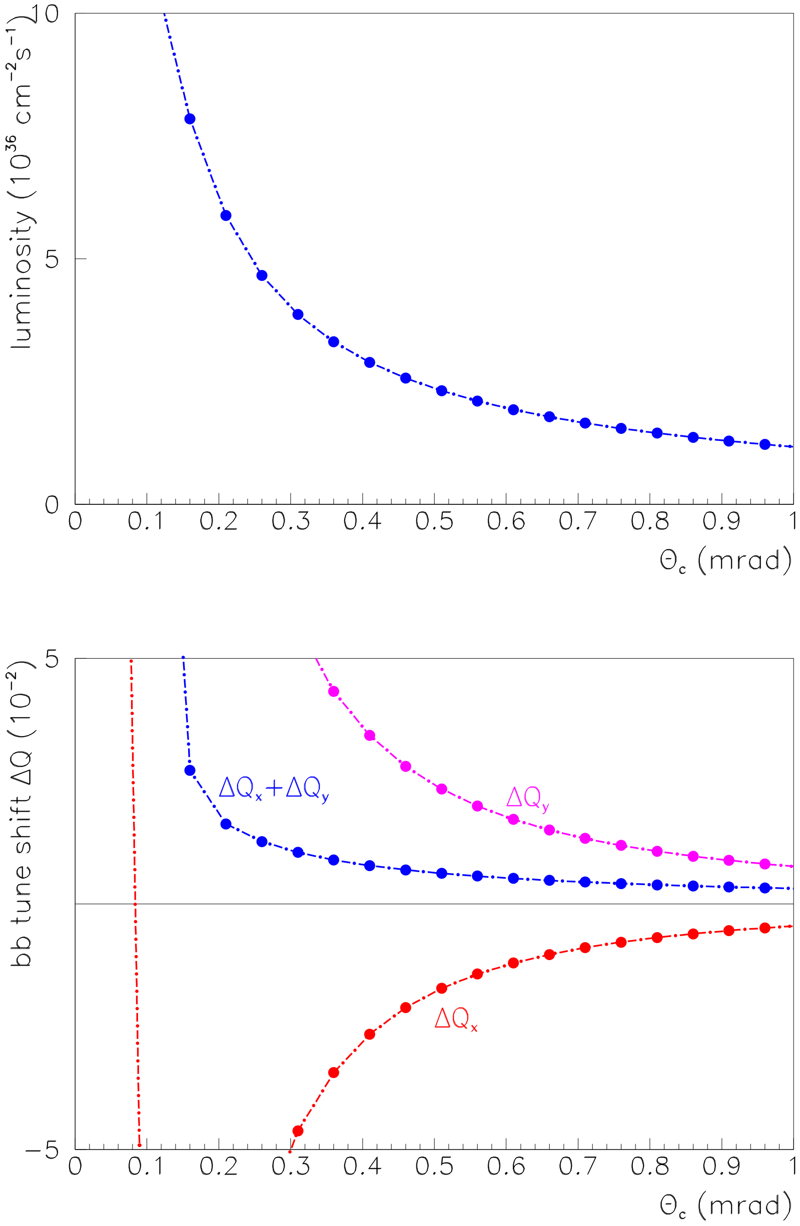

Fig. 39. Luminosity (top) and total beam-beam tune shifts (bottom) vs. crossing angle, for a continuous beam with a line density $\lambda = 8.8 \times 10^{11}$ m^{-1} (40 A current), $\beta^* = 0.25$ m, $l_{\rm det} = 1$ m, $l = 20$ m, and $\gamma\epsilon_\perp = 3.75$ μm.

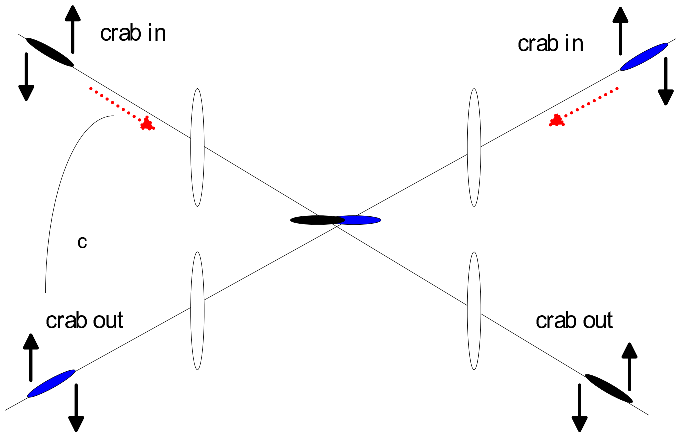

Fig. 40. Applying a deflection of opposite sign to the head and tail of each bunch avoids luminosity loss due to the crossing angle.

crossing is illustrated in Fig. 40. The differential deflection received in the dipole cavities aligns the bunches at the collision point, so that the luminosity is the same as for head-on collisions.

The crab cavities would be most useful if they would allow separating the beams after the collision into two disjoint quadrupoles. Assuming that the distance between the last quadrupole and the IP remains about 20 m, and considering an outer quadrupole radius of 25 cm, a scheme with two separate final quadrupoles requires a minimum crossing angle of $\theta_c \geq 25$ mrad. The corresponding transverse crab deflecting voltage is

$$V_\perp = \frac{cE \tan\theta_c/2}{e\omega_{\rm rf}\sqrt{\beta_x^*\beta_x^{\rm crab}}} \ , \tag{43}$$

where E is the beam energy, $\omega_{\rm rf}$ the angular rf frequency, and $\beta_x^{\rm crab}$ the beta function at the cavity.

Table 12 compares the crab-cavity parameters required for such type LHC upgrade with those designed for the KEK B factory. The LHC requires about 100 times more deflecting voltage, primarily due to the increased beam energy. Note also that the rf frequency of 1.3 GHz chosen would be too high for the present nominal LHC bunch length.

Table 12. Comparison of crab cavities parameters for KEKB with those for an advanced LHC upgrade.

variable	symbol	KEKB HER	LHC
beam energy	E	8.0 GeV	7 TeV
RF frequency	$f_{\rm rf}$	508.9 MHz	1.3 GHz
half crossing angle	$\theta_c/2$	11 mrad	12.5 mrad
IP beta function	β_x^*	0.33 m	0.25 m
cavity beta function	$\beta_x^{\rm crab}$	100 m	2000 m
required kick voltage	$V_\perp$	1.44 MV	144 MV

3.3 Stronger Magnets

In order to reach a higher energy in the LEP/LHC tunnel, stronger magnets are absolutely needed. These stronger magnets would also be in line with the historial trend, evidenced in Fig. 2. There exist s.c. magnet materials which can sustain much higher fields and current densitities than NbTi, the material used so far for all accelerator magnets. A candidate material which could approximately double the maximum field of the magnets is Nb_3Sn. Table 13 summarizes the historical evolution of the field strengths achieved in Nb_3Sn magnets. Nb_3Sn is more brittle than NbTi, which complicates the cable fabrication and the processing procedures, but recent progress bodes well for the future.

3.4 Emittance Evolution

The synchrotron radiation amplitude damping time is[75]

$$\tau_z J_z = \left(\frac{3(m_p c^2)^3}{e^2 c^3 r_p Z^2}\right) \frac{1}{B^2 E} \left(\frac{C}{2\pi\rho}\right) \approx \frac{16644\text{hr}}{E[\text{TeV}] B[\text{T}]^2} \left(\frac{C}{2\pi\rho}\right) \frac{A^4}{Z^4}. \tag{44}$$

The damping decrement is defined as

$$\delta = \frac{T_0}{n_{\rm IP}\tau_{x,y}} \approx 5.7 \times 10^{-13}\, E[\text{TeV}]^2 B[\text{T}] \frac{Z^3}{A^4} \tag{45}$$

where we have assumed $n_{\rm IP} = 2$ interaction points.

Radiation damping could improve the beam-beam limit, a hypothesis which is supported by the much higher tune shifts achieved in electron-positron colliders as com-

Table 13. Evolution of Nb_3Sn Magnets.[74]

year	group	type	field/gradient
1982	CERN	quad	71 T/m
1983	CERN/Saclay	dipole	5.3 T
1985	LBL	dipole D10	8 T
1986	KEK	dipole	4.5 T
1988	BNL	dipole	7.6 T
1991	CERN-ELIN	dipole	9.5 T
1995	LBNL	hybrid dipole D19H	8.5 T
1995	UT-CERN	dipole MSUT	11.2 T
1996	LBNL	dipole D20	13.3 T
2001	LBNL	common coil dipole	14.4 T

pared with hadron colliders. Measurements and simulations have been fitted by[76]

$$\xi_{\max} \propto 0.009 + 0.021\,(\delta/10^{-4})^{0.5}. \tag{46}$$

Figure 41 illustrates this dependence. Superimposed on the curve representing Eq. (46) are data from hadron colliders and from LEP. The points for the future hadron colliders were chosen on top of the predicted curve. The figure demonstrates that even for the next and the next-to-next generations of hadron colliders, the damping decrement is still too small to noticably enhance the maximum beam-beam tune shift.

A more important consequence of synchrotron radiation is the shrinkage of the emittance during the store. As mentioned earlier the situation is still different from electron storage rings, as the damping time is of the order of hours and not milliseconds.

The equilibrium emittance due to synchrotron radiation is[75]

$$\epsilon_{x,N}^{\mathrm{SR}} \approx \frac{55}{32\sqrt{3}}\frac{\lambda\!\!\!^{-}_A}{J_x}\left(\frac{\gamma^3}{Q_\beta^3}\right)\left(\frac{C}{2\pi\rho}\right)^3 . \tag{47}$$

For both LHC-II and VLHC, this 2–3 orders smaller than the design emittance, implying the possibility of excessive beam-beam forces, and the generation of beam halo and background.

However, an equilibrium emittance of much larger value will be reached much earlier, namely at the time when the radiation damping is balanced by intrabeam scattering.

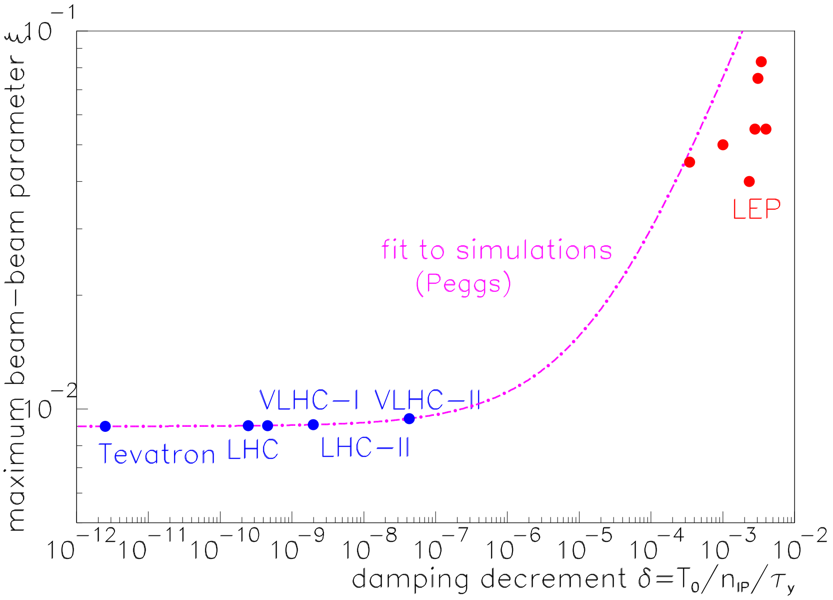

Fig. 41. Tune shift parameter vs. damping decrement. (LEP data courtesy of R. Assmann; LEP was not beam-beam limited)

The beam size growth rate from intrabeam scattering is[77]

$$\frac{1}{\tau_{x,\rm IBS}} \approx \frac{c r_p^2 N_b L_c}{16 Q \epsilon_{x,N}^2 \sqrt{\kappa}\sqrt{\kappa+1}\,\gamma\sigma_z\sigma_\delta} \tag{48}$$

where $L_c \approx 20$. Asymptotically, for $\gamma \gg Q_\beta$, one expects that $1/\tau_{\delta,\rm IBS} \approx 1/\tau_{x,\rm IBS}$ and $\sigma_\delta \approx Q_\beta^{3/2}\sqrt{\epsilon_x/\rho}$.[77] Equating the intrabeam-scattering growth rate and the radiation damping yields the following expression for the equilibrium emittance[78]:

$$\epsilon_{x,N}^{\rm IBS} = \frac{\rho^{5/6} N_b^{1/3}}{Q_\beta \gamma^{7/6}} \left(\frac{Z f_{\rm rf} e V_{\rm rf}}{cE\kappa(\kappa+1)}\right)^{1/6} \left(\frac{C}{2\pi\rho}\right)^{1/6} \left(\frac{3 r_p L_c}{16}\right)^{1/3}, \tag{49}$$

where $f_{\rm rf}$ denotes the rf frequency, $V_{\rm rf}$ the total rf voltage, $\kappa = \epsilon_y/\epsilon_x$ the asymptotic emittance ratio as determined by linear coupling and spurious vertical dispersion.

To give a concrete example, we take the LHC-II parameters of Table 3. Note that these assume $\kappa = 1$, which can be achieved by skew qudrupoles and/or a proper choice of betatron tunes. Figure 42 shows the predicted emittance variation as a function of time, and Figs. 43, 44, and 45 the bunch population, beam-beam tune shift, and luminosity, respectively. The result is encouraging: the luminosity initially stays high and almost constant, while the beam-beam tune shift only slowly and moderately increases.

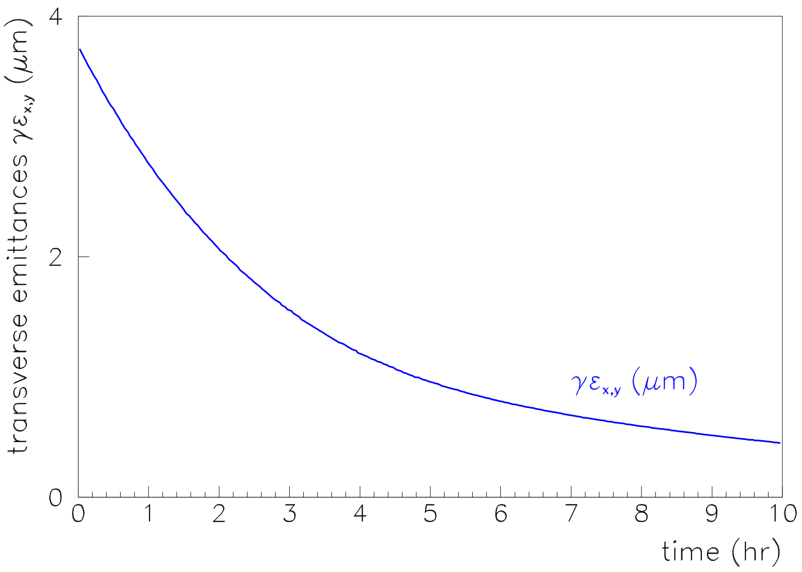

Fig. 42. Evolution of transverse emittance vs. time in LHC-II at 28 TeV centre-of-mass energy, for the parameters of Table 3. The simulation includes synchrotron radiation damping, intrabeam scattering, and particle consumption in the collision.

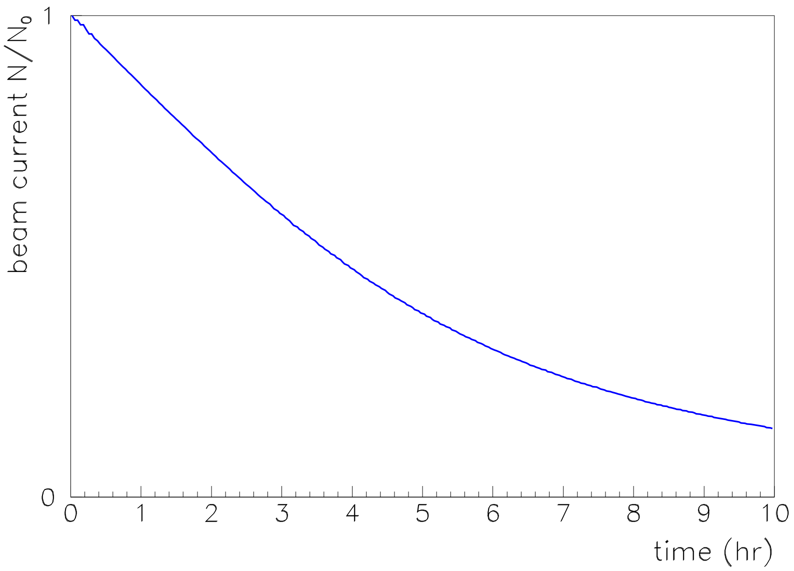

Fig. 43. Evolution of beam current vs. time in LHC-II at 28 TeV centre-of-mass energy, for the parameters of Table 3.

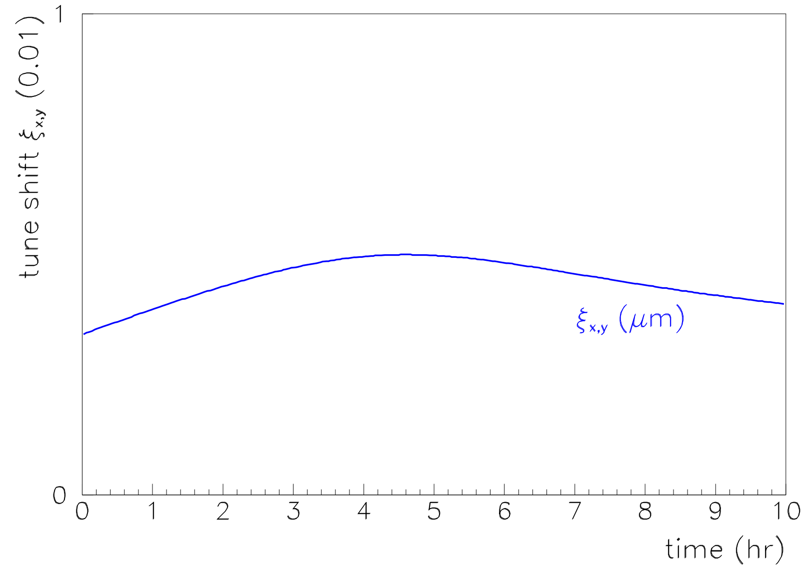

Fig. 44. Evolution of beam-beam tune shift vs. time in LHC-II at 28 TeV centre-of-mass energy, for the parameters of Table 3.

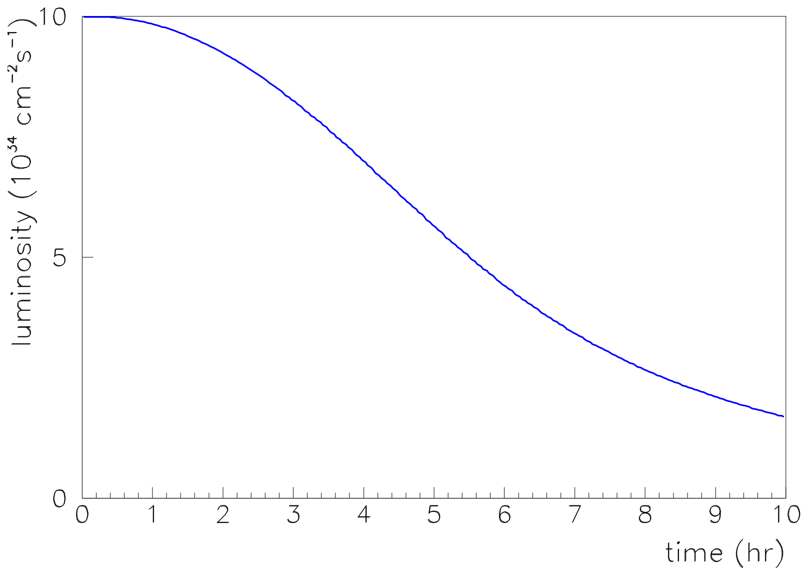

Fig. 45. Evolution of luminosity vs. time in LHC-II at 28 TeV centre-of-mass energy, for the parameters of Table 3.

3.5 Collective Effects

One of the most harmful collective effects is the loss of Landau damping for higher-order longitudinal modes. If the bunch becomes too short the frequency spread due to the nonlinearity of the rf decreases, and Landau damping may be lost. The condition for stability is

$$\sigma_s \geq \frac{C}{2\pi}\left[\frac{\pi^3}{6}\frac{N_b f_{\rm rev} e}{h_{\rm rf}^3 V_{\rm rf}}\,{\rm Im}\left(\frac{Z_L}{n}\right)_{\rm eff}\right]^{1/5} . \tag{50}$$

Figure 46 shows that in the contemplated scenario for LHC-II Landau damping would be lost after about 3 hours. Longitudinal noise excitation[79] could maintain a minimum bunch length and thereby stabilize the beam, as is illustrated in Fig. 47.

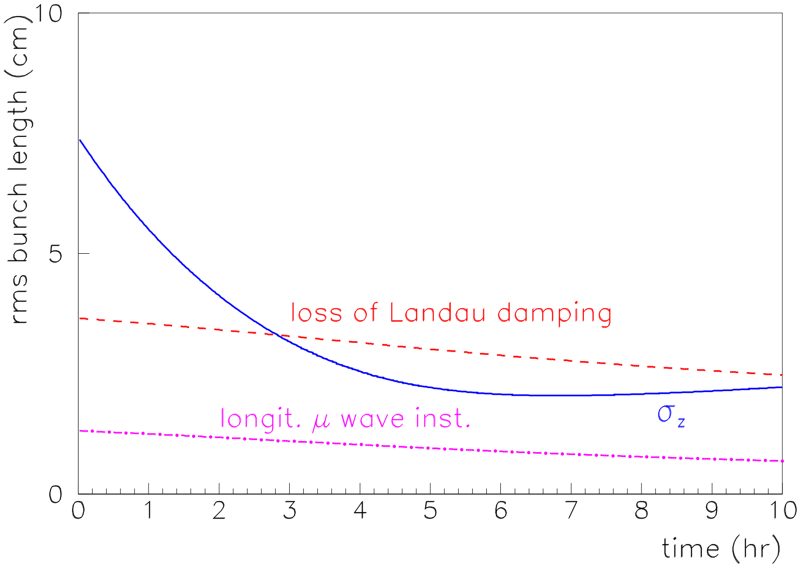

Fig. 46. Evolution of the rms bunch length during a store in LHC-II, and the instability thresholds for ${\rm Im}(Z_L/n)_{\rm eff} \approx 0.1\ \Omega$ (as estimated for LHC), for 28 TeV centre-of-mass energy, and the parameters of Table 3.

As for the LHC, other collective effects that may occur are the longitudinal microwave instability, the transverse coupled-bunch resistive-wall instability, and the electron cloud.

Figure 48 displays the simulated arc heat load in the LHC due to the electron cloud as a function of bunch spacing. For bunch spacings shorter than the nominal, the heat load can easily increase by an order of magnitude. Only when the spacing becomes

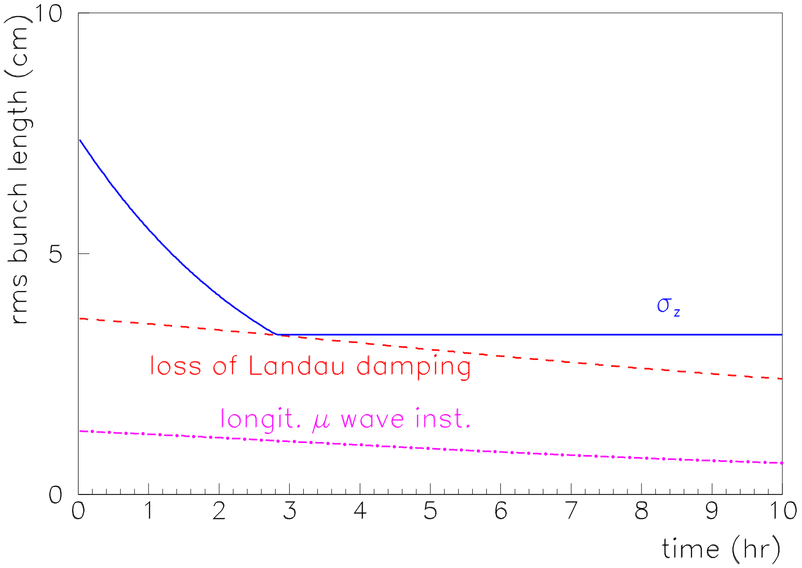

Fig. 47. Evolution of the rms bunch length during a store in LHC-II, and the instability thresholds for $\mathrm{Im}(Z_L/n)_{\mathrm{eff}} \approx 0.1\ \Omega$ (as estimated for LHC) when after 3 hours rf noise is added to maintain a constant longitudinal emittance of $\epsilon_L \geq 0.104$ eVs.

comparable to the bunch length, and we approach the limit of a coasting beam, does the heat load again decrease.

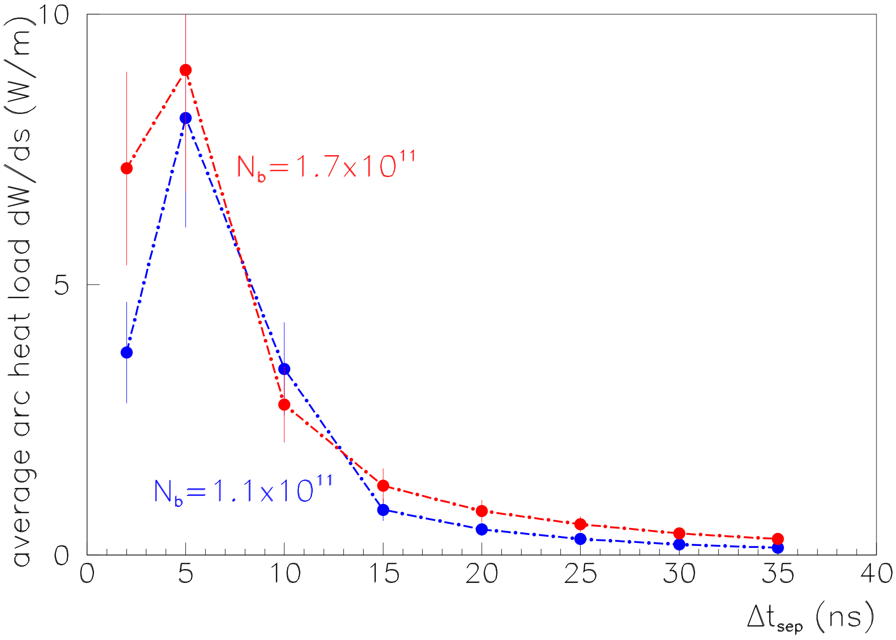

Fig. 48. Average LHC arc heat load as a function of bunch spacing, for a maximum secondary emission yield of $\delta_{\rm max} = 1.1$, a beam energy of 7 TeV, and two different bunch populations N_b.

3.6 Total Current and Synchrotron Radiation

The total beam current could be limited either by magnet quenches due to gas scattering, or by the maximum tolerable synchrotron radiation power,

$$P_{\rm SR} = \frac{C_\gamma E^4 N_b n_b c}{C\rho} = U_0 f_{\rm rev} n_b N_b, \tag{51}$$

where U_0 denotes the energy loss per turn, and $C_\gamma = 4\pi/3\ r_p/(m_p c^2)^3 \approx 0.778 \times 10^{-17}\ {\rm m/GeV}^3$ (m_p is the proton mass, and r_p the classical proton radius). Using the expressions for the luminosity and the beam-beam tune shift, Eq. (51) can be rewritten as[75]

$$P_{\rm SR} = \left(\frac{8\pi r_p^{3/2}}{\sqrt{3cE_A}} \right) \frac{\kappa}{1+\kappa^2} \frac{E^{3/2} L \beta_x^*}{\xi \sqrt{J_z \tau_z}} \sqrt{\frac{C}{2\pi\rho}}\ . \tag{52}$$

This implies the following scaling.[80] If the magnetic field is held constant, then $J_z\tau_z \propto 1/E$ and the radiation power increases as $P_{\rm SR} \propto E^2 L$. On the other hand, if the magnetic field follows the historical evolution, $B \propto E^{1/2}$, we obtain $J_z\tau_z \propto 1/E^2$ and the power grows as $P_{\rm SR} \propto E^{5/2} L$. In the next generation of hadron colliders, the power per unit length deposited by synchrotron radiation is already of the order of 1 W/m, and this scaling indicates much higher power levels for the machines which follow.

It is not easy and rather inefficient to absorb this energy inside the magnets at a temperature of a few Kelvin, even using a beam screen. For the VLHC, P. Bauer et al. have proposed a more efficient scheme, which is based on discrete warm photon-stops inserted into the beam pipe.[81] Such photon stops would considerably improve the efficiency and could reduce the wall plug power required for cooling by an order of magnitude. However, the stops have to be retracted at injection and they contribute to the beam-pipe impedance.

3.7 The VLHC

The VLHC design study has made great progress recently,[82] and a complete report has been published before Snowmass 2001.[7] The VLHC circumference is almost 10 times that of LHC, and the costs are kept low, by staging the project, and by economizing the magnets. The first stage uses 2-T magnets, whose design comprises a small 100-kA superconducting transmission line surrounded by the beam pipe and by warm iron yokes, which determine the shape of the field. The operating margin of several such designs has been verified in a 100-kA test loop at Fermilab.

A single tunnel can house the stage-1 magnets, and at a later time the higher-field stage-2 magnets, which will increase the centre-of-mass energy to values close to 200-TeV.

A complete site layout has been proposed, adjacent to the Tevatron, the latter serving as an injector. The layout foresees two collision points, both close to the Fermilab site, and it includes a bypass line for the lower-energy stage-1 ring around the detectors, which is needed, once the stage-2 is operational.

4 Conclusions

Hadron colliders have performed exceedingly well in the past. The LHC will break new territory. With 14 TeV centre-of-mass energy, and a luminosity of 10^{34} cm^{-2}s^{-1}, it will surpass all previous colliders. The LHC design is based on the experience gained at the ISR, SPS, the Tevatron, HERA, RHIC, and other machines. The underlying assumptions are rather conservative.

Yet, the accelerator physicists face various exciting challenges, *e.g.*, related to magnet design, cryogenics, long-range beam-beam collisions, strong-strong beam-beam collisions, radiation damping — which for the first time is stronger than intrabeam scattering —, and the electron cloud.

Beyond the nominal LHC, studies have started on LHC luminosity and energy upgrades. A more ambitious 2-stage Very Large Hadron Collider has been proposed in the US. The second stage of the VLHC could reach an energy of 175 TeV in the centre of mass. The problems confronted by these future projects include the development of new magnets with either higher field or much reduced production costs, the possibly large circumference, the increased synchrotron radiation, and again the electron cloud. A further new development are ‘quasi-continuous’ beams or superbunches. These might provide a path towards significantly higher luminosity. They may also allow for a reduced beam-beam tune shift, suppress the electron-cloud build up and avoid PACMAN bunches, *i.e.*, bunches with unfavorable long-range collisions.

In conclusion, profiting from enhanced synchrotron radiation, the LHC upgrades and the VLHC hold the promise of further substantial advancements in energy and luminosity at sustainable power levels and costs.

Acknowledgements

I would like to thank the organizers for inviting to me to lecture at this school and the participants for enlightening and lively discussions. I also thank G. Arduini, R. Assmann, P. Bagley, P. Bauer, F. Bordry, L. Bottura, D. Brandt, O. Brüning, I. Collins, K. Cornelis, A. Faus-Golfe W. Fischer, J. Gareyte, O. Gröbner, H. Grote, G. Guignard, W. Herr, J.B. Jeanneret, J.M. Jimenez, C. Johnstone, J. Jowett, E. Keil, J.-P. Koutchouk, K.-H. Mess, K. Ohmi, S. Peggs, F. Pilat, B. Richter, L. Rossi, F. Ruggiero, G. Rumolo, F. Schmidt, R. Schmidt, E. Shaposhnikova, V. Shiltsev, M. Syphers, T. Taylor, R. Thomas, A. Verdier, L. Vos, J. Wei, and many others for material, inspiration, and helpful comments.

References

[1] E. Keil, CERN 72-14, 1972.

[2] A. Hofmann et al., CERN ISR-OP-TH/80-19, 1980.

[3] L. Evans, 1987 IEEE PAC, Washington, 1987; M. Harrison, R. Schmidt, EPAC 88 Nice, 1988; V. Hatton, 1991 IEEE PAC, San Francisco, 1991.

[4] G. Dugan, 14th HEACC, Tsukuba, 1989.

[5] K. Ohmi, Phys. Rev. Lett. 75, 1526, 1995; F. Zimmermann, CERN LHC PR 95, 1997; O. Gröbner, IEEE PAC97 Vancouver; K. Ohmi, F. Zimmermann, Phys. Rev. Lett. 85, 3821, 2000; G. Rumolo et al., PRST-AB 012801, 2001; CERN SL workshops Chamonix X & XI, 2000 and 2001.

[6] S. Klein, LBL-PUB-45566, 2000; J.B. Jeanneret, SL/AP Beam Physics Note 41; D. Brandt, LHC Project Report 450, 2000.

[7] See web site *http://vlhc.org*

[8] A.G. Ruggiero, *Hadron Colliders at Highest Energies and Luminosities*, World Scientific, Singapore, 1998.

[9] P. Bagley, private communication (2001).

[10] A. Chao, S. Peggs, R. Talman, presentations at Mini-Workshop: “The effect of synchrotron radiation in the VLHC,” BNL, Sept. 18–20, 2000.

[11] The web page of the LHC project is *http://wwwlhc.cern.ch*

[12] Proceedings of the Chamonix workshops X and XI are accessible at *http://cern.web.cern.ch/CERN/Divisions/SL/news/news.html*

[13] Accelerator Physics Group of the CERN SL Division at *http://wwwslap.cern.ch*

[14] O. Brüning, private communication (2001).

[15] L. Bottura, Proc. Chamonix X, p. 238, CERN-SL-2000-007 DI (2000); Proc. Chamonix XI, p. 238, CERN-SL-2001-003-DI (2001).

[16] E. Keil, private communication (2001).

[17] W. Herr, “Effects of PACMAN bunches in the LHC,” LHC Project Report 39 (1996).

[18] J. Irwin, SSC-233 (1989).

[19] Y. Papaphilippou and F. Zimmermann, PRST-AB **2**, 104001 (1999).

[20] F. Zimmermann, CERN LHC Project Note 250 (2001).

[21] F. Ruggiero and F. Zimmermann, "Luminosity Optimization by Increasing Bunch Length or Crossing Angle," report in preparation.

[22] J.-P. Koutchouk, Proc. IEEE PAC 2001 Chicago (2001).

[23] V.D. Shiltsev et al., PRST-AB, 2:071001,1999

[24] R.E. Meller, R.H. Siemann, IEEE Trans. Nucl. Sci. **28**, p. 2431 (1981)

[25] K. Yokoya, Y. Funakoshi, E. Kikutani, H. Koiso, J. Urakawa, KEK-PREPRINT-89-14 (1989).

[26] O. Brüning, private communication (2001).

[27] A.W. Chao and B. Zotter, 'Landau Damping,' in 'Handbook of accelerator physics and engineering', by A.W. Chao (ed.), M. Tigner (ed.), Singapore (1999).

[28] Y. Alexahin, CERN-SL-96-064-AP (1996).

[29] M.P. Zorzano and F. Zimmermann, PRST-AB **3**, 044401 (2000).

[30] Y. Alexahin, H. Grote, W. Herr, M.-P. Zorzano, Proc. HEACC'01 Tsukuba (2001).

[31] F. Ruggiero, CERN SL/95-09, 1995.

[32] J.T. Rogers, CBN 96-14, 1996.

[33] J. Gareyte, CERN SL-Note-2000-056 AP (2000).

[34] V. Lebedev, VLHC miniworkshop, SLAC March 2001.

[35] M. Blaskiewicz et al., VLHC miniworkshop, SLAC March 2001. SLAC-PUB-8800 (2001).

[36] L.R. Evans, IEEE PAC New York (1999).

[37] F. Bordry, Proc. Chamonix XI, p. 250, CERN-SL-2001-003-DI (2001).

[38] D. Cocq, O.R. Jones, H. Schmickler, 8th Beam Instrumentation Workshop, SLAC, USA, CERN SL-98-062 BI (1998).

[39] F. Schmidt, R. Tomas, A. Faus-Golfe, Proc. IEEE PAC 2001 Chicago (2001).

[40] F. Sonnemann, Ph.D. Thesis, CERN-THESIS-2001-004 (2001).

[41] J.B Jeanneret, Chamonix X, CERN-SL-2000-007 DI (2000).

[42] K.H. Mess, R. Schmidt, Proc. Chamonix XI, p. 284, CERN-SL-2001-003-DI (2001).

[43] J.M. Zazula and S. Péraire, LHC Project Report 112 (1997).

[44] J. Jowett, Proc. LHC99 beam-beam workshop, CERN/SL/99-039 AP, p. 63 (1999).

[45] W. Herr, H. Grote, in LHC Project Report 502 (2001).

[46] R. Garoby, Proc. Chamonix XI, p. 32, CERN-SL-2001-003-DI (2001).

[47] R. Cappi et al., Proc. Chamonix XI, p. 29, CERN-SL-2001-003-DI (2001).

[48] T. Bohl et al., CERN SL-Note-2001-040 MD (2001).

[49] G. Arduini et al., PAC 2001, Chicago (2001).

[50] G. Arduini, Chamonix XI, CERN-SL-2001-003 DI (2001).

[51] O. Gröbner, HEACC'77, Protvino (1977).

[52] V. Baglin et al, Electron Emission of Copper," LHC-Project-Report-472 (2001).

[53] O. Gröbner, "Beam induced multipacting," IEEE PAC 97, Vancouver (1997).

[54] F. Zimmermann, Proc. PAC'2001 Chicago, USA, CERN-SL-2001-035 (AP) (2001).

[55] F. Zimmermann, in Proc. Chamonix X, CERN-SL-2000-007 (2000); Chamonix XI, CERN-SL-2001-003-DI (2001).

[56] O. Gröbner, private communication (2000).

[57] W. Höfle, Chamonix X, CERN-SL-2000-007-DI (2000).

[58] G. Rumolo and F. Zimmermann, Proc. Int. workshop in Two-Stream Instabilities," KEK Tsukuba (2001).

[59] B. Richter, SLAC memo, unpublished (2000).

[60] G. Rumolo and F. Zimmermann, Proc. Int. Workshop on Two-Stream Instabilities," KEK Tsukuba (2001).

[61] G. Rumolo, F. Zimmermann, H. Fukuma, K. Ohmi, Proc. PAC'2001 Chicago, USA, and CERN-SL-2001-040 (AP) (2001).

[62] K. Ohmi, F. Zimmermann, Phys. Rev. Lett. 85, 3821, 2000;

[63] K. Ohmi, F. Zimmermann, E. Perevedentsev, HEACC2001, Tsukuba, Japan, and CERN-SL-2001-011 AP (2001).

[64] K. Cornelis, Chamonix XI, CERN-SL-2001-003-DI.

[65] G. Rumolo, F. Zimmermann, Proc. PAC’2001 Chicago, USA, and CERN-SL-2001-041 (AP) (2001).

[66] F. Zimmermann, LHC Project-Report 95, and SLAC-PUB-7425 (1997).

[67] V. Baglin et al., LHC-Project-Report-472 (2001).

[68] J.M. Jimenez, ‘The SPS as Vacuum Test Bench for the Electron Cloud Studies with LHC Type Beams,’ August 2001.

[69] F. Ruggiero (ed.) et al., ‘Feasibility Study of LHC Luminosity and Energy Upgrades,’ report in preparation (2001).

[70] J. Gareyte, private communication (2001).

[71] K. Takayama, J. Kichiro, M. Sakuda, M. Wake, ‘Superbunch Hadron Colliders,’ submitted to Physical Review Letters (2001).

[72] F. Ruggiero, private communication (2001).

[73] R. Palmer, ‘Energy Scaling, Crab Crossing, and the Pair Problem,’ in the DPF Summer Study Snowmass ‘88, ‘High Energy Physics in the 1990s,’ SLAC-Pub-4707 (1988).

[74] A. den Ouden, U. of Twente, CERN LHC Seminar (2001).

[75] E. Keil, Proc. PAC 97, p. 104, 1996, and Proc. 34th Eloisatron Workshop, Erice 1996.

[76] E. Keil and R. Talman, Particle Accelerators vol. 14, 1993; S. Peggs, LHC99 beam-beam workshop, Geneva, 1999; R. Assmann and K. Cornelis, EPAC 2000 Vienna, 2000.

[77] J. Wei, “Intrabeam Scattering Scaling for Very Large Hadron Colliders,” unpublished draft (2001); J. Bjorken and S. Mtingwa, Part. Acc. 13, 115 (1983).

[78] F. Zimmermann, Proc. HEACC’2001 , Tsukuba, Japan, CERN-SL-2001-009 AP (2001).

[79] T. Toyama et al., Proc. EPAC 2000, Vienna; similar methods were used at the S$p\bar{p}$S by T. Linnecar.

[80] F. Zimmermann, HEACC2001, Tsukuba, Japan, CERN-SL-2001-009 AP (2001).

[81] P. Bauer, et al., IEEE PAC 2001 Chicago (2001).

[82] M. Syphers, S. Peggs, M4 Group Summary Talk at Snowmass 2001.